

# Identifying mergers using non-parametric morphological classification at high redshifts

Robert Thompson<sup>1,2,3</sup>, Romeel Davé<sup>2,4,5</sup>, Shuiyao Huang<sup>6</sup>, Neal Katz<sup>6</sup>

<sup>1</sup> *NCSA, University of Illinois, Urbana-Champaign, IL 61820*

<sup>2</sup> *University of the Western Cape, Bellville, Cape Town 7535, South Africa*

<sup>3</sup> *Astronomy Department, University of Arizona, Tucson, AZ 85721, USA*

<sup>4</sup> *South African Astronomical Observatories, Observatory, Cape Town 7925, South Africa*

<sup>5</sup> *African Institute for Mathematical Sciences, Muizenberg, Cape Town 7945, South Africa*

<sup>6</sup> *Astronomy Department, University of Massachusetts, Amherst, MA 01003, USA*

2 August 2018

## ABSTRACT

We investigate the time evolution of non-parametric morphological quantities and their relationship to major mergers between  $4 \geq z \geq 2$  in high-resolution cosmological zoom simulations of disk galaxies that implement kinetic wind feedback,  $H_2$ -based star formation, and minimal ISM pressurisation. We show that the resulting galaxies broadly match basic observed physical properties of  $z \sim 2$  objects. We measure the galaxies' concentrations ( $C$ ), asymmetries ( $A$ ), and *Gini* ( $G$ ) and  $M_{20}$  coefficients, and correlate these with major merger events identified from the mass growth history. We find that high values of asymmetry provide the best indicator for identifying major mergers of  $> 1 : 4$  mass ratio within our sample, with *Gini*- $M_{20}$  merger classification only as effective for face-on systems and much less effective for edge-on or randomly-oriented galaxies. The canonical asymmetry cut of  $A \geq 0.35$ , however, is only able to correctly identify major mergers  $\sim 10\%$  of the time, while a higher cut of  $A \geq 0.8$  more efficiently picks out mergers at this epoch. We further examine the temporal correlation between morphological statistics and mergers, and show that for randomly-oriented galaxies, half the galaxies with  $A \geq 0.8$  undergo a merger within  $\pm 0.2$  Gyr, whereas *Gini*- $M_{20}$  identification only identifies about a third correctly. The fraction improves further using  $A \geq 1.5$ , but about the half the mergers are missed by this stringent cut.

**Key words:** galaxies:evolution, galaxies:formation, galaxies:high-redshift, galaxies:structure, galaxies:general, methods:numerical

## 1 INTRODUCTION

A key to understanding galaxy evolution is the ability to interpret their morphologies. Galaxies are believed to grow and evolve via in-situ star formation, major and minor mergers, and gas accretion from the intergalactic and circumgalactic medium. Understanding a galaxy's morphology provides an important avenue for understanding how these processes are responsible for establishing the observed structural features of the galaxy population across cosmic time (Conselice 2014), such as the origin and emergence of the present-day Hubble sequence.

Visual classification along the Hubble sequence has a long history as a valuable descriptor of galaxy properties. Morphology is observed to correlate with many other properties such as colour, star formation rate, surface brightness, and gas content. However, visual classification remains ultimately subjective. Hence there has been much interest in developing quantitative classification schemes. Surface bright-

ness profiles (de Vaucouleurs 1948; Sérsic 1963) provide such an avenue for quantitatively characterising the light distribution. Such parametric characterisations must nonetheless make assumptions about the underlying functional form that may not hold for all stages of galaxy formation. For instance, they are less well-defined in the case of merging or other irregular galaxies.

More recently, non-parametric methods have gained popularity for quantifying morphology. In this case, the pixelised image is directly characterised into a mathematical form. Some common methods in use today are the Concentration-Asymmetry-Clumpiness (CAS) system (Conselice et al. 2003), the *Gini* ( $G$ ) coefficient, and the second-order moment of the brightest 20% of a galaxy's pixels ( $M_{20}$ ) (Lotz et al. 2004). Since these non-parametric quantities do not make any assumptions about the underlying form of galactic structure, they are considered a less biased tool

to identify objects that are undergoing key transformative events such as mergers.

Major mergers are thought to play an important role in the evolution of galaxies. In addition to transforming the morphology towards earlier type (e.g. Toomre & Toomre 1972; Cox et al. 2008), they are believed to be responsible for generating bursts of star formation (Mihos & Hernquist 1996; Narayanan et al. 2010b,a) as well as stimulating rapid growth of the central supermassive black hole (Sanders & Mirabel 1996). While it is now clear despite the resulting starbursts, such mergers do not dominate the cosmic star formation at any observable epoch (e.g. Rodighiero et al. 2011), nonetheless their importance to galaxy transformation and black hole growth makes the identification of mergers a key challenge in forming a complete picture for the emergence of the galaxy population.

While non-parametric morphologies offer a model-independent approach to characterising mergers, they must be calibrated against other schemes, typically visual classification, to interpret them. This can be most easily done at low redshifts, where the galaxies can be well-resolved and are thus straightforward to classify. In this way, CAS and *Gini-M*<sub>20</sub> have been shown to isolate mergers in particular regions of parameter space. Using this, CAS has been used to identify major merger candidates in numerous galaxy surveys (e.g. Abraham et al. 1996; Conselice et al. 2003; Cassata et al. 2005; Menanteau et al. 2006). Lotz et al. (2004) argued that *Gini-M*<sub>20</sub> is more effective at identifying late-stage mergers and classifying low-redshift galaxies.

As galaxy surveys are extended to higher redshifts, such parametrisations continue to be utilised to classify mergers and morphologies. With surveys such as CANDELS (Grogin et al. 2011; Koekemoer et al. 2011) using *Hubble*, the morphology of distant galaxies can be resolved at rest-optical wavelengths, which if interpreted properly could provide important information towards understanding the evolution of galaxies during the peak epoch of cosmic star formation. However, visual morphologies of high-redshift galaxies do not clearly follow the Hubble sequence classification seen today. For example, at  $z \sim 2$  disks tend to be thicker, more turbulent, and clumpier (e.g. Förster Schreiber et al. 2009; Elmegreen et al. 2009; Genzel et al. 2011), ellipticals are substantially more compact (van Dokkum et al. 2014), and the fraction of irregulars increases substantially compared to today. It is thus not clear how well non-parametric morphologies calibrated at low- $z$  will apply to such distant galaxies, and hence whether quantitative morphology can be effectively utilised to characterise the high- $z$  galaxy population.

Cosmological hydrodynamical simulations provide a promising avenue to better understand how quantitative morphologies relate to key evolutionary events in galaxies such as mergers. With improving spatial resolution and a better understanding of the basic physical ingredients required to broadly reproduce observed galaxies (Somerville et al. 2015), they have emerged as a valuable complementary tool to elucidate the physical processes that shape galaxies. With sophisticated analysis tools, simulated galaxies can be processed into mock observations that may be analysed in an analogous fashion to real data, with the advantage that the true underlying distribution of the mass, light, and metals is known.

Lotz et al. (2008) investigated both CAS and *Gini-*

*M*<sub>20</sub> statistics for a number of mock observed non-cosmological, isolated, merging systems in hydrodynamic simulations. It was found that *Gini-M*<sub>20</sub> identified mergers at their first passage and when the system finally coalesced, but did not consistently identify mergers at intermediate times. Lotz et al. (2008, 2010b,a) further went on to characterise the time-scales for structural mergers for *A* and *Gini-M*<sub>20</sub> to be of similar order. These simulations were used to calibrate the *Gini-M*<sub>20</sub> merger identification relation for observed galaxies out to  $z > 3$ .

A different approach was taken by Cibinel et al. (2015), who classified mergers using resolved stellar maps as opposed to single-band images. They found that a combination of *A* and *M*<sub>20</sub> measured on the stellar mass maps of  $\sim 100$  HUDF galaxies provided the most accurate distinction between mergers and isolated clumpy galaxies. They found that merger samples identified on the basis of *A* from a single *H - band* image resulted in a contamination as high as  $\sim 50\%$  from clumpy galaxies, and argue that their method reduces this contamination.

While informative, isolated galaxy simulations such as those used in these studies do not capture the cosmological context of galaxy formation. They lack crucial ingredients such as the frequent infall of smaller satellites (i.e. minor mergers), and important avenues for galaxy growth by smooth accretion (which is believed to be the dominant fuelling mode; Kereš et al. 2005). Given that the merger and accretion rates are much higher in the past than today, morphology could be strongly impacted by such processes.

More recently, the focus has shifted towards using cosmological zoom-in simulations, in which an individual galaxy and its environs are evolved at much higher resolution relative to the entire volume. This retains the full cosmological context while making feasible the high resolution needed to study internal structural processes within galaxies such as violent disk instabilities (Dekel et al. 2009). Snyder et al. (2015) examined the *Gini-M*<sub>20</sub> statistics for a number of high-resolution zoom-in galaxies at  $3 > z > 1$ . They found that *Gini-M*<sub>20</sub> was more sensitive to early stages of mergers ( $t < 0$ ). Overall they concluded that structural evolution is neither universal nor monotonic, and that *Gini-M*<sub>20</sub> were largely sensitive to viewing angle, star formation, and mergers.

In this paper we examine a number of galaxies at  $4 \geq z \geq 2$  within high-resolution cosmological smoothed particle hydrodynamic zoom-in simulations. We mock observe our galaxy sample as if they were detected in the *H - band* CANDLES survey with *HST* and investigate their *C*, *A*, *G*, and *M*<sub>20</sub> values as a function of their mass histories. Our primary aim is to determine the optimal approach for quantifying the merger history of galaxies using non-parametric morphological statistics. The hope is that this will provide a better understanding of how such statistics can best be used to interpret the evolution of galaxies at early epochs.

This paper is organised as follows: in §2 we describe our simulations and the methods. §3 examines the global properties of our galaxy sample. §4 looks at the morphological statistics, while §5 investigates the morphological statistics of each galaxy as a function of cosmic time. Finally in §6 we summarise our conclusions.

## 2 METHODS

### 2.1 Simulation Code

Our simulations are evolved with an extended version of the GADGET-3 cosmological SPH code (Springel 2005; Huang et al. 2015). It includes cooling processes using the primordial abundances described in Katz et al. (1996), with additional cooling from metal lines assuming photo-ionisation equilibrium from Wiersma et al. (2009). We account for metal enrichment from Type II supernovae (SNe), Type Ia SNe, AGB stars, and we track four elements (C,O,Si,Fe) individually as described in Oppenheimer & Davé (2008). Galactic outflows are implemented using the hybrid energy/momentum-driven wind (ezw) model fully detailed in Davé et al. (2013) and Ford et al. (2015).

Compared to our previous code described in Oppenheimer & Davé (2008), we now use the ‘pressure-entropy’ SPH algorithm that better handles issues of two-phase instabilities when compared to the standard ‘density-entropy’ SPH formulations (see Saitoh & Makino 2013; Hopkins 2013, for further details). Following Hopkins (2013) we use a standard quintic spline kernel with 128 neighbours and adopt the Morris & Monaghan (1997) artificial viscosity along with a Balsara (1989) switch. We also implement a time-step limiter (Saitoh & Makino 2009; Durier & Dalla Vecchia 2012) that improves the accuracy of the time integration scheme in situations where there are sudden changes to a particle’s internal energy.

To suppress artificial fragmentation within the interstellar medium, we prevent gas particles from cooling below their effective Jeans temperature (Katz & Gunn 1991; Schaye & Dalla Vecchia 2008; Robertson & Kravtsov 2008) by ensuring that the simulation is always resolving at least one Jeans mass within a particle’s smoothing length. This translates to a threshold number density for pressurisation of

$$\rho_{th} = \frac{3}{4\pi} \left( \frac{5kT}{G} \right)^3 \left( \frac{1}{N_{ngb} m_{gas}} \right)^2, \quad (1)$$

where  $T = 10^4\text{K}$ ,  $m_H$  is the mass of a hydrogen atom,  $k$  is the Boltzmann constant,  $N_{ngb}$  is the number of neighbours within an SPH kernel, and  $m_{gas}$  is the mass of an individual gas particle within the simulation (one Jeans mass here is  $N_{ngb}m_{gas}$ ). Particles with densities above  $\rho_{th}$  and are considered to be multi-phase, and a Jeans temperature floor is imposed

$$T_{Jeans} = 10^4 (\rho/\rho_{th})^{4/3}, \quad (2)$$

where  $\rho$  is the gas particle’s density. In low-resolution simulations,  $\rho_{th}$  can drop below the nominal star formation threshold of  $n = 0.13\text{cm}^{-3}$ , in which case we set it to this value; however, in the zoom simulations presented in this work, this does not occur. The net effect is analogous to adding ISM pressure (Springel & Hernquist 2003), but rather than directly pressurising the gas, we prevent the gas from cooling and thus fragmenting below the Jeans scale. The net effect of this implementation is in practice quite similar to that of Schaye & Dalla Vecchia (2008), who force gas particles to lie on the  $T \propto \rho^{4/3}$  relation, except that rather than using a fixed density threshold (as they use), we adjust our density threshold  $\rho_{th}$  to naturally increase as the resolution of the simulation increases. This minimises the

amount of artificial pressure introduced into the ISM, which more accurately captures the internal structure of galaxies while suppressing fragmentation on scales that we cannot resolve.

To model star formation, we employ a molecular gas-based prescription. The molecular content ( $f_{H_2}$ ) of each gas particle is calculated following the analytic model of Krumholz et al. (2008, 2009, hereafter KMT) and McKee & Krumholz (2010); details can be found in Thompson et al. (2014). We stochastically form stars from the gas following a Schmidt (1959) Law as in

$$\dot{\rho}_* = \epsilon_* f_{H_2} \frac{\rho}{t_{ff}}. \quad (3)$$

The efficiency of star formation  $\epsilon_*$  is set to 1% per local free-fall time  $t_{ff}$  (Krumholz & Tan 2007; Lada et al. 2010). This model allows us to regulate star formation using the local abundance of  $H_2$  rather than the total gas density, which confines star formation to the densest peaks in the ISM as is typically seen in real galaxies, thereby preserving the ISM structure as much as the numerical resolution allows. This also introduces a metallicity dependence into the star formation efficiency, since the KMT model of molecular gas formation relies on the presence of dust, which may be important for suppressing early star formation (Tassis et al. 2012; Krumholz et al. 2012).

### 2.2 Initial Conditions

Initial conditions are generated using the MUSIC code (Hahn & Abel 2011) assuming a flat  $\Lambda$ CDM cosmology. Cosmological parameters are chosen to be consistent with constraints from the Planck Collaboration et al. (2013) results, namely  $\Omega_m = 0.3$ ,  $\Omega_\Lambda = 0.7$ ,  $H_0 = 70$ ,  $\sigma_8 = 0.8$ ,  $n_s = 0.96$ .

Our target halos are selected at  $z = 2$  from a low-resolution hydrodynamic simulation consisting of  $256^3$  dark-matter and gas particles in a  $(16h^{-1}\text{Mpc})^3$  volume with an effective comoving spatial resolution of  $\epsilon_{grav} = 1.25h^{-1}\text{kpc}$ , which is  $417h^{-1}\text{pc}$  at  $z = 2$ . We populate each target halo with higher resolution particles at  $z = 249$ , with the size of each higher resolution region chosen to be 2.5 times the maximum radius of the original halo from the low-resolution hydrodynamic simulation. The majority of halos in our sample are simulated with a single additional level of refinement ( $\epsilon_{grav} = 625h^{-1}\text{pc}$  or  $208h^{-1}\text{pc}$  at  $z = 2$ ), while the two lowest mass halos are simulated with two additional levels of refinement ( $\epsilon_{grav} = 313h^{-1}\text{pc}$  or  $104h^{-1}\text{pc}$  at  $z = 2$ ).

Our six selected halos produce seven massive central galaxies at  $z = 2$  that have no low-resolution particles within their virial radius. The galaxies span halo masses of  $2 \times 10^{11} - 10^{12} M_\odot$ , stellar masses of  $3.6 \times 10^9 - 6.6 \times 10^{10} M_\odot$ , and star formation rates (SFRs) from  $5 - 60 M_\odot/\text{yr}$ . We label them in order of increasing halo mass, and their global properties at  $z = 2$  are listed in Table 1. Note that given the stellar masses of our sample at  $z = 2$ , it is likely that each of these galaxies will end up as an elliptical galaxy more massive than the Milky Way by  $z = 0$  (Lu et al. 2014, 2015).

### 2.3 Simulation analysis with SPHGR

We perform the simulation analysis using the recently developed open-source python package **Smoothed Particle**

Table 1. Simulated Galaxy Sample at  $z = 2$ 

Name	Symbol	$M_{\text{halo}}$	$M_{\star}$	SFR	$f_{\text{gas}}$
G1	■	$1.91 \times 10^{11}$	$3.57 \times 10^9$	4.93	0.54
G2	●	$1.98 \times 10^{11}$	$7.77 \times 10^9$	9.96	0.47
G3	▲	$3.35 \times 10^{11}$	$9.49 \times 10^9$	8.77	0.57
G4	◆	$4.85 \times 10^{11}$	$1.80 \times 10^{10}$	2.51	0.44
G5	●	$9.55 \times 10^{11}$	$4.05 \times 10^{10}$	19.93	0.39
G6	◆	$1.15 \times 10^{12}$	$5.58 \times 10^{10}$	37.50	0.21
G7	▼	$1.03 \times 10^{12}$	$6.64 \times 10^{10}$	59.04	0.28

Note. — Halos used throughout this work along with their central galaxies. All were selected from a low resolution simulation in a  $(16h^{-1}\text{Mpc})^3$  volume. The smallest two halos (G1 and G2) have a comoving spatial resolution of  $\epsilon_{\text{grav}} = 313h^{-1}$  pc ( $208h^{-1}$  pc at  $z = 2$ ), while the rest (G3-G7) have  $\epsilon_{\text{grav}} = 625h^{-1}$  pc ( $104h^{-1}$  pc at  $z = 2$ ).  $M_{\text{halo}}$  and  $M_{\star}$  are given in units of  $M_{\odot}$ , while SFRs are given in units of  $M_{\odot}\text{yr}^{-1}$ .

**Hydrodynamics Galaxy Reduction**, or SPHGR<sup>1</sup> (Thompson 2015). In its most basic form, the code is responsible for running a baryonic group finder to identify galaxies, a halo finder to identify dark matter halos, assign galaxies to their respective halos, calculate halo and galaxy global properties, and finally iterate through previous time steps to identify the most-massive progenitors of each halo and galaxy. Information about each individual halo and galaxy is collated in a convenient, intuitive, and easy-to-access manner that eliminates unnecessary overhead in the analysis process.

We use SKID<sup>2</sup> (Spline Kernel Interpolative Denmax) to identify galaxies as bound groups of baryonic particles (Governato et al. 1997; Stadel 2001). All of the galaxies presented in this work are well above our nominal 64 star particle resolution limit (Finlator et al. 2006). To identify dark matter halos and the associated baryonic particles we use the six dimensional phase space halo finder ROCKSTAR-GALAXIES<sup>3</sup> (Behroozi et al. 2013). By considering particle velocities, ROCKSTAR can much more accurately identify distinct groups of particles in mergers when compared to conventional FOF methods (e.g. Thompson et al. 2015).

After the identification of galaxies and halos via the above methods, SPHGR creates individual python objects for each halo and galaxy. These objects contain basic statistical information such as mass and radius, and additionally the member lists of gas, star, and dark matter (DM) particles (for halos) that belong to each object. For each SKID galaxy, SPHGR assigns halo membership by cross-correlating galaxy membership information with halo membership to determine which halo has the most number of particles contributing to that galaxy. The most massive galaxy within each halo is classified as the ‘central’, while all others are classified as ‘satellites’. We calculate the HI content of each galaxy using the auto-shielding approximation as detailed in Davé et al. (2013), along with global properties such as the stellar mass,  $H_2$  gas mass, star formation rate (SFR), and SFR-weighted metallicity.

SPHGR identifies the primary progenitors of each galaxy and

halo throughout previous time steps, as follows. For each halo we identify the halo in the previous output that contains the most dark matter particles from the current halo as the main progenitor. In the case of galaxies, we utilise star particles rather than dark matter particles to track progenitors in a similar manner.

## 2.4 LOSER

To create mock observations of our galaxies, we employ our newly developed code LOSER (Line Of Sight Extinction by Ray-Tracing) to compute the emission spectrum and magnitude maps, i.e. images, for each galaxy.

LOSER uses the Flexible Stellar Population Synthesis library (FSPS; Conroy et al. 2009; Conroy & Gunn 2010) to generate single stellar population spectra interpolated to each simulated star particle’s age and metallicity. Each star’s spectrum is individually extinguished based on the integrated dust column by computing a line-of-sight metal column density to the star towards a user-specified direction, using an SPH kernel-weighted integral of particles along the LOS. The metal column is converted to  $A_V$  using relations measured for the Milky Way (Watson 2011) at solar metallicity and above, while a metallicity-dependent dust-to-metal ratio is used at lower metallicities based on high- $z$  GRB measurements (De Cia et al. 2013). Given  $A_V$ , an extinction law is then applied; here we use a Calzetti et al. (2000) law. LOSER also accounts for IGM attenuation based on Madau (1995), and nebular emission lines, though the former is unimportant for the bands we consider, and the latter does not play a significant role at the redshifts we consider.

The attenuated stellar spectra are then grouped into pixels of a user-specified size. User-selected band passes are then applied to obtain rest- or observed-frame magnitudes in each pixel. In our case, we select our pixel size to correspond to  $0.03''$  at the appropriate redshift of the simulation output, which is comparable to the pixel scale in drizzled (Koekemoer et al. 2003) Wide Field Camera 3 (WFC3) images from *Hubble*. The image is then blurred according to the diffraction limit of the incoming wavelength; e.g. for the case of F160W on WFC3 we apply a Gaussian smoothing to the image with a FWHM of  $\sim 0.05''$ .

LOSER accurately estimates the emergent flux in bands where reprocessed dust emission does not dominate, e.g. all the rest-ultraviolet to near-infrared bands that we consider here. LOSER does not predict a spectrum for the far-infrared reprocessed emission (though it does output the bolometric reprocessed luminosity) as would be predicted using a full dust radiative transfer code such as SUNRISE (Jonsson 2006), but it is much faster and provides greater user control over its input quantities such as the extinction law.

## 3 GLOBAL PROPERTIES

To characterise our galaxy sample and ensure that they are broadly in accord with observations, we first examine the evolution of their global properties between  $4 \geq z \geq 2$ .

### 3.1 Mass histories

We begin by examining the mass growth histories of our galaxies, and describe how we identify major mergers. First, galaxies are linked at  $z = 2$  with their most massive progenitor in previous outputs as described in §2.3. This allows for the extraction of each galaxy’s baryonic mass history, and hence we can identify at each output (redshift) a merger ratio  $\mathcal{R}$  defined by

$$\mathcal{R} \equiv \frac{M_1}{M_2} = \frac{M_t - M_{(t-1)}}{M_t}, \quad (4)$$

<sup>1</sup> <https://bitbucket.org/rthompson/sphgr>

<sup>2</sup> <http://www-hpcc.astro.washington.edu/tools/skid.html>

<sup>3</sup> <https://bitbucket.org/pbehroozi/rockstar-galaxies>

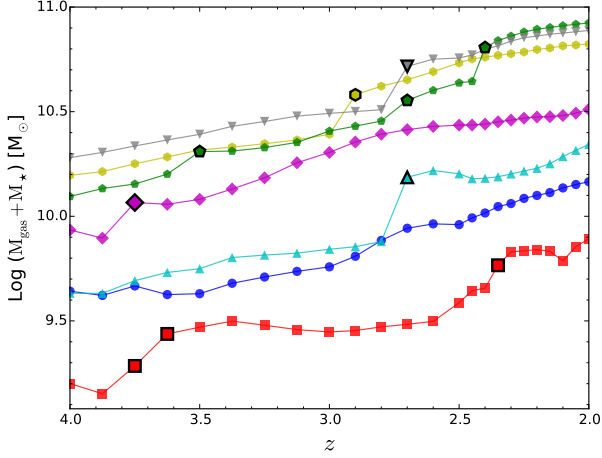


**Figure 1.** Evolution of the total baryonic mass ( $M_{gas} + M_*$ ) of each galaxy within our sample between redshifts  $4 \geq z \geq 2$ . The end of major mergers ( $M_1/M_2 \geq 1/4$ ) are indicated by data points with black borders.

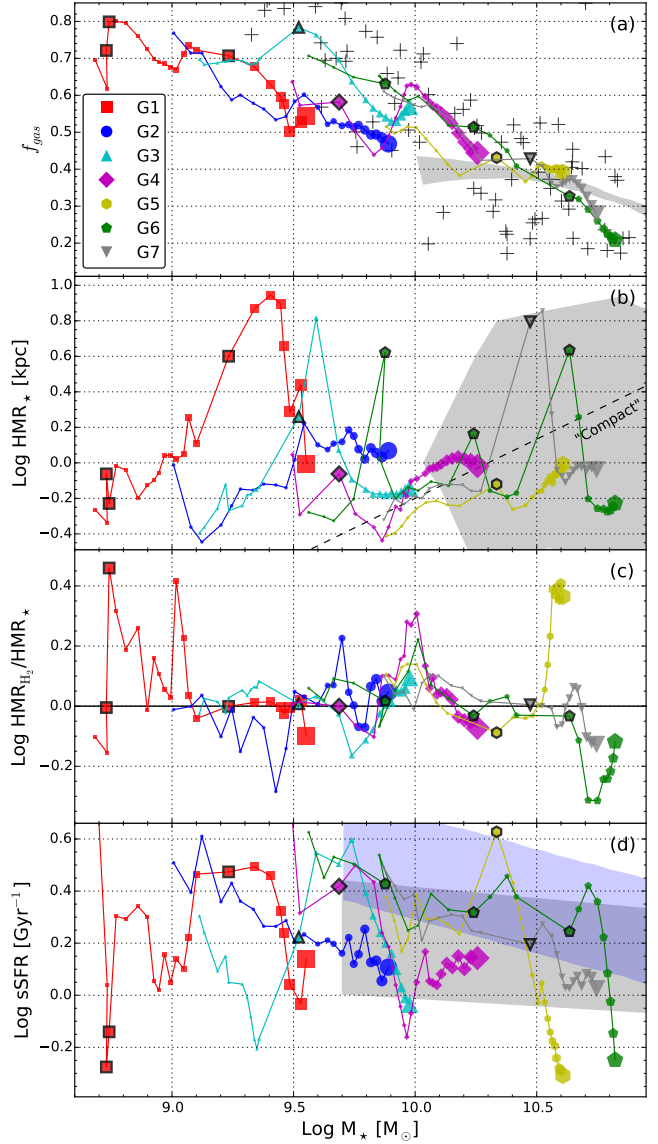
where  $M_t$  is the mass of the galaxy at the current output, and  $M_{(t-1)}$  is the galaxy’s mass in the previous output (outputs have an approximate spacing of  $\Delta t \approx 50 - 100$  Myr). We consider merger ratios of at least 1:4 ( $\mathcal{R} \geq 0.25$ ) to be major mergers. We will not explicitly discuss minor mergers, but canonically this is specified by  $\mathcal{R} \geq 0.1$ . A histogram of  $\mathcal{R}$  values within our sample separates into two components, one that peaks at  $\mathcal{R} \sim 0.03$  and another that peaks at  $\mathcal{R} \sim 0.4$ , with a dip around  $\mathcal{R} \sim 0.25$ . Hence our major merger cut at  $\mathcal{R} \geq 0.25$  is chosen to isolate this separate population of events that is distinct from just an extension of typical “smooth” accretion and minor mergers.

Figure 1 displays the total baryonic mass ( $M_{gas} + M_*$ ) history of each galaxy within our sample. The ending time of identified major mergers are indicated by large symbols with black borders. The overall mass history of these galaxies is dominated by relatively smooth growth (Murali et al. 2002; Kereš et al. 2005), but major mergers occur in all galaxies but one (G2) over this redshift range. There are a total of 10 major mergers that occur within our sample between  $4 \geq z \geq 2$ , yielding a typical timescale between mergers of  $\sim 1.25$  Gyr.

### 3.2 Gas fraction

The gas fraction ( $f_{gas} \equiv M_{gas}/(M_{gas}+M_*)$ ) history of our galaxies is shown in Figure 2(a), again with the end of major mergers shown as points with black borders for reference. Overall, the gas fraction evolves downwards with time. As discussed in Davé et al. (2011), this owes to efficient outflows in small galaxies at early epochs that keeps galaxies from converting gas into stars. After major mergers, we often see a somewhat more rapid decrease in  $f_{gas}$ , suggesting that these galaxies consume the gas available for star formation quickly during these events.

The predicted values of  $f_{gas}$  between  $4 \geq z \geq 2$  for our galaxies broadly agree with the Erb et al. (2006)  $z = 2$  observations shown as grey crosses, with galaxies evolving mostly down along the relation with time. This indicates that the ISM gas content of our galaxies is generally in accord with observed galaxies at these epochs. It is, however, somewhat higher than the gas fractions in the lower redshift  $z \approx 1 - 1.5$  PHIBBS data (shown as the grey contour; Tacconi et al. 2013).



**Figure 2.** Redshift evolution of global properties of our galaxy sample between  $4 \geq z \geq 2$ . Major mergers ( $\mathcal{R} \geq 1/4$ ) are again indicated by data points with black borders. Panel (a) shows  $f_{gas}$  for each galaxy, with observational data at  $z = 2$  as the grey crosses (Erb et al. 2006), and  $z = 1 - 1.5$  data from PHIBBS (Tacconi et al. 2013) as the grey contour. Panel (b) shows the half-mass radius for each galaxy, the ‘compactness’ line for  $1.4 < z < 3$  (Barro et al. 2013), and  $1 < z < 3$  observational data compiled by Bruce et al. (2012) as the grey contour. Panel (c) shows the ratio of the molecular gas half-mass radius and the stellar half mass radius for each galaxy, the ‘compactness’ line for  $1.4 < z < 3$  (Barro et al. 2013), and  $1 < z < 3$  observational data compiled by Bruce et al. (2012) as the grey contour. Panel (d) shows the specific star formation rate for each galaxy with the grey contour representing observational data at  $z = 2$  (Daddi et al. 2007; Krumholz et al. 2012), and the blue contour from Speagle et al. (2014). Panel (d) shows the specific star formation rate for each galaxy with the grey contour representing observational data at  $z = 2$  (Daddi et al. 2007; Krumholz et al. 2012), and the blue contour from Speagle et al. (2014).

### 3.3 Size

Figure 2(b) shows the stellar half-mass radius ( $\text{HMR}_\star$ ) of each of our galaxies between  $4 \geq z \geq 2$ . Galaxies typically have sizes around 1 physical kpc at all epochs, and show no obvious trend with mass. The weak evolution of galaxy size with respect to stellar mass is in broad agreement with numerical models and observations out to  $z \sim 1$  (e.g. Somerville et al. 2008; Brooks et al. 2011). Our galaxy sizes also lie within the locus of  $3 > z > 1$  observations shown as the grey contour (Bruce et al. 2012). We note that our physical resolution (i.e. gravitational softening length) at these epochs is generally better than  $\sim 200$  pc, so these galaxies are all reasonably well-resolved.

We also overlay the  $3 > z > 1.4$  line that delineates “compact” galaxies from Barro et al. (2013). Identifying the progenitors of massive compact galaxies has been a topic of great interest recently (e.g. Barro et al. 2013; Patel et al. 2013; Stefanon et al. 2013; Wellons et al. 2015; Zolotov et al. 2015; Fang et al. 2015; Stringer et al. 2015; Graham et al. 2015). In our simulations, galaxies grow much more slowly in half-mass radius than in stellar mass; in this plot they tend to move nearly horizontally with time. As a result, the three most massive galaxies (G7, G6, G5) all end up in the compact regime. G4 undergoes an early merger that lowers its radius into the compact regime at a low mass, but it quickly re-grows out of being compact, then nearly returns to becoming compact by  $z = 2$ .

Mergers often greatly but temporarily increase the size. This may be because SKID will often identify two merging galaxies as a single one prior to final coalescence, resulting in a large half-mass extent. However, by the next output the galaxy usually settles back to something similar to its previous size. In detail, the final radius tends to be slightly smaller than the pre-merger one (though not always). Nonetheless, it is not obviously the case that major mergers are primarily responsible for driving galaxies into the compact regime. Instead, the primary driver seems to be simply the fact that galaxy growth in stellar mass is not accompanied by a sizeable increase in radius at these epochs, which thus eventually drives galaxies into the compact regime.

A separate question is what process removes the star-forming gas once it reaches the compact regime to produce red and dead compact ellipticals as observed (van Dokkum & Brammer 2010). We cannot address this question directly in our simulations since we do not include a model for quenching star formation. Nonetheless, if such quenching is associated with the presence of massive ( $M_h \gtrsim 10^{12} M_\odot$ ) halos filled with hot gas as is often speculated (e.g. Croton et al. 2006; Gabor & Bournaud 2014), then it may be that galaxies coincidentally achieve sufficiently massive halos roughly at approximately the same stellar mass where their radii move into the compact regime. In such a scenario, most quenched galaxies would start out as compact, although the exact fraction depends on the stochasticity in the relationship between quenching and halo mass (or whatever the governing parameter might be). We leave a more detailed study of this for future work.

### 3.4 Gas radius

Figure 2(c) shows the ratio of the molecular (star-forming) gas half-mass radius and the stellar half-mass radius. Overall, the two evolve together showing, as expected, that the stars form where the gas is located. However, there are some interesting departures. Shortly after a merger, G4’s molecular half-mass radius increases to twice its stellar half-mass radius, before settling back down in size. This mostly owes to the stellar radius dropping just prior, suggesting a scenario where internal dynamical effects condense the core before gas falls back in to regrow a larger disk, which then forms stars allowing the stellar radius to catch up. Such effects have been seen in isolated merger simulations where the progen-

itors are gas-rich (Robertson et al. 2004) as well as cosmological zoom simulations of early galaxy growth (Governato et al. 2007).

Another interesting case is G5, where just before  $z = 2$  its gas radius shoots up to more than twice its stellar radius. Again, this happens not too long after a merger when the stellar radius drops a bit, suggesting a similar scenario of ongoing disk regrowth. This suggests that if the molecular gas radius can be measured, e.g. using ALMA, and compared to the stellar radius from *HST*, outliers in this relation may identify galaxies that have recently undergone internal dynamical evolution via a merger, and are in the phase of disk re-growth.

### 3.5 Specific star formation rate

In Figure 2(d) we plot the specific star formation rate ( $\text{sSFR} \equiv \text{SFR}/M_\star$ ) of our sample, with the grey contour representing  $z \approx 2$  observational data from Daddi et al. (2007), and the blue contour representing a fit to observations by Speagle et al. (2014).

Galaxies generally show a mild downward evolution in sSFR as a function of  $M_\star$ . For the vast majority of the time, all our galaxies lie within the observed range, which evolves slowly at  $z \gtrsim 2$  (e.g. Krumholz et al. 2012; Stark et al. 2013; Duncan et al. 2014; Speagle et al. 2014). At the final redshift, all the galaxies but G5 and G6 lie within the range of the observations. This is a non-trivial success that is difficult to achieve in lower-resolution simulations (Davé 2008; Sparre et al. 2015; Somerville et al. 2015), and suggests that the higher resolution, and potentially the inclusion of a molecular hydrogen-based star formation prescription, is important for obtaining sufficiently high sSFRs at  $z \sim 2$ .

For G5 and G6, these galaxies mostly evolved within the observed range, but experienced fairly sudden drops in sSFR just prior to  $z = 2$ . This was preceded by a mild increase in sSFR associated with a merger event. The drop in sSFR occurs along with a rise in the ratio of the gas to stellar radius. Hence for these objects a plausible scenario is, as discussed earlier, that they underwent a merger and consumed their dense gas, and are now regrowing a gas disk that has not yet achieved a sufficient mass or density to restart vigorous star formation. These may be examples of the sort of “quenching” discussed in Feldmann & Mayer (2015), but it is not quenching in the conventional sense that results in red-and-dead galaxies, since eventually the gas accretion will likely re-invigorate star formation (e.g. Gabor et al. 2010).

In summary, our galaxies lie within the range of typical observed galaxies at  $z \sim 2$  in terms of their gas content, size, and specific SFR. Hence they provide a plausible set of objects with which to examine morphological characteristics and their correlation with merger history.

## 4 MORPHOLOGICAL STATISTICS

We now examine non-parametric morphological statistics for our galaxies at  $4 \geq z \geq 2$ . Every galaxy in Table 1 is processed through LOSER six times for each of our 24 outputs between  $4 \geq z \geq 2$ ; three correspond to random orientations aligned with the axes of our simulation box, while the other three are composed of a face-on orientation, and two edge-on orientations separated by  $90^\circ$ . These viewing angles will be represented by the colours cyan (random), blue (face-on), and red (edge-on), respectively. This results in 144 mock observations for each of our seven galaxies, or 1,008 total mock observations for our entire sample.

We focus here on the F160W band as the reddest WFC3 band that provides the most direct correlation with stellar mass. We have also repeated this analysis using the F814W band of ACS, which falls in the rest-frame ultraviolet, but the statistics

and correlations we obtain are not substantially different and the resulting conclusions remain the same; hence we do not discuss F814W further here. We will discuss detailed properties of colour variations in future work, and confine ourselves here to the F160W images for calculating our non-parametric morphological statistics.

#### 4.1 Basic morphological characteristics

To set the stage, Figure 3 shows face-on processed images from LOSER for each galaxy in our sample at  $z = 2$ . The three columns show the gas, star formation rate, and stellar surface densities, respectively, while the final two columns show the extinguished LOSER images in the WFC3 H-band (F160W) the ACS I-band (F814W) filters. The flux from images like these are used to calculate their morphological statistics in the following sections. The white bar at the bottom of each image represents a scale of 5 physical kpc.

Overall, the gas surface densities clearly indicate a disk-like morphology, albeit with significant levels of disturbance evident owing to ongoing minor mergers. The SFR generally follows the densest gas, mainly occurring in gas with  $\Sigma_{\text{gas}} > 10^7 M_{\odot} \text{kpc}^{-2}$  in accord with the Kennicutt (1998) relation. The stellar component does not show as obvious a disk-like morphology, though we have checked that they do show rotation. The stellar map also shows evidence for ongoing merging activity, most strongly in the smaller galaxies such as G2. The gas disks are quite extended compared to the stars, reaching 20 kpc across.

In the mock images, even at *HST*'s resolution, many of the small-scale features in these galaxies are washed out. Nonetheless, the fact that G2 is about to undergo a merger clearly remains evident; interestingly, this is the only one of our galaxies that does not show an identified merger from  $4 < z < 2$ . Spiral arms are barely if at all evident. They are most apparent in G5, which resembles the grand design spiral seen by Law et al. (2012).

#### 4.2 Concentration and Asymmetry

A basic morphological parameter of a galaxy is its light concentration ( $C$ ). This has long been used to morphologically characterise galaxies in various classification schemes (e.g. Morgan & Mayall 1957). It has also been used extensively to quantify trends in local galaxies (e.g. Bershady et al. 2000; Conselice et al. 2003). Higher values of  $C$  mean that a larger amount of the galaxy's light is contained within the central region. Concentration is typically defined as the ratio of light within a circular radii containing 20% ( $r_{20}$ ) and 80% ( $r_{80}$ ) of the total galaxy flux (Conselice et al. 2003):

$$C = 5 \log \left( \frac{r_{80}}{r_{20}} \right). \quad (5)$$

The concentration is calculated using pixels within  $1.5r_p$  where  $r_p$  is the Petrosian radius, which we define as the radius of a circular aperture where the flux at that radius is 20% of the flux within that radius (e.g., Bershady et al. 2000; Conselice et al. 2003).

Asymmetry ( $A$ ) is another common morphological statistic that quantifies the rotational symmetry of a galaxy (Abraham et al. 1996; Brinchmann et al. 1998; Conselice et al. 2003). It is measured by rotating the image by  $180^\circ$  and subtracting that from the original image (Abraham et al. 1996; Conselice et al. 2000):

$$A = \frac{\sum |f_0 - f_{180}|}{\sum |f_0|}, \quad (6)$$

where  $f_0$  is the original image pixel flux values, and  $f_{180}$  is the rotated image's pixel flux, and the sum is over all pixels within  $1.5r_p$ . Higher values of  $A$  correspond to higher degrees of asymmetry, which can be used to identify merger-candidates. Conselice

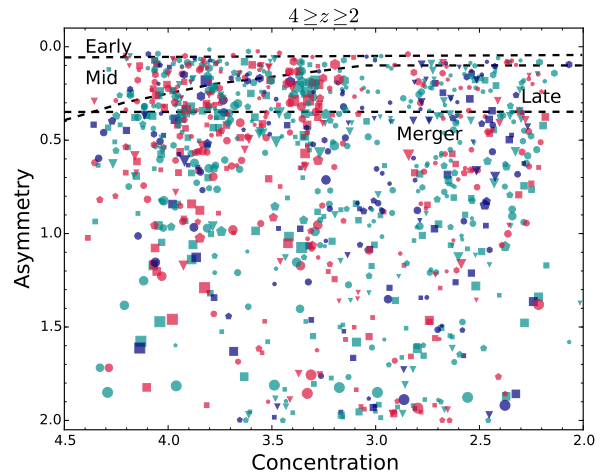


**Figure 4.** Asymmetry  $A$  as a function of Concentration  $C$  for our sample between  $4 \geq z \geq 2$ . Each galaxy in our sample contains 6 data points: 3 random viewing orientations (cyan), 2 edge-on views separated by  $90^\circ$  (red), and one face-on view (blue). Point size corresponds to the specific star formation rate (sSFR) of each galaxy, with smaller points representing smaller sSFRs. Dashed lines correspond to regions in which different galaxy types are typically found in the local universe (Bershady et al. 2000; Conselice et al. 2003).

et al. (2003, 2008), for example, set a threshold value of  $A \geq 0.35$  for major mergers based on their studies of nearby galaxies in various phases of evolution. They focused on numerous different data sets that included normal galaxies, starburst galaxies, dwarf irregulars, dwarf ellipticals, and galaxies undergoing a merger.

$C$  and  $A$  are traditionally plotted against each other to classify a galaxy's morphology and merger state. Figure 4 shows  $C$  vs.  $A$  for our 1,008 mock observations between  $4 \geq z \geq 2$ . The lines indicate the region in which different galaxy types are typically found in the local universe (Bershady et al. 2000; Conselice et al. 2003), and the point sizes are representative of each galaxy's sSFR.

Within our sample we find a median concentration of 3.3, and a median asymmetry of 0.49. Hence using the canonical definition that identifies mergers as objects with  $A \geq 0.35$ , the median galaxy at  $z = 2 - 4$  in our sample is a merger. Given that major mergers are not that frequent as shown in our mass history plots, this indicates that the canonical value, tuned for lower-redshift galaxies, is not straightforwardly applicable at higher redshifts. We will examine this more quantitatively later.

Examining each of these quantities individually allows us to investigate potential correlations with the merger ratios extracted from the simulation (§3). We split our data into three groups corresponding to the face-on, edge-on, and random viewing angles. Random orientation is the most directly relevant when comparing to the full sample of objects in a galaxy survey, but it may be possible to isolate a sample of face-on or edge-on objects for comparison to the other panels. Two power laws are fit to the data within each panel; one with no weighting (blue), and the other weighted by the galaxy's sSFR (orange). The sSFR weighting can potentially assist merger identification since mergers tend to have higher sSFRs, and it is also information typically available in a multi-wavelength galaxy survey. Each panel's legend shows the power-law index of each fit along with the uncertainty in the slope.

Figure 5 shows the merger ratio as a function of the concentration of each galaxy for each viewing orientation. The horizontal

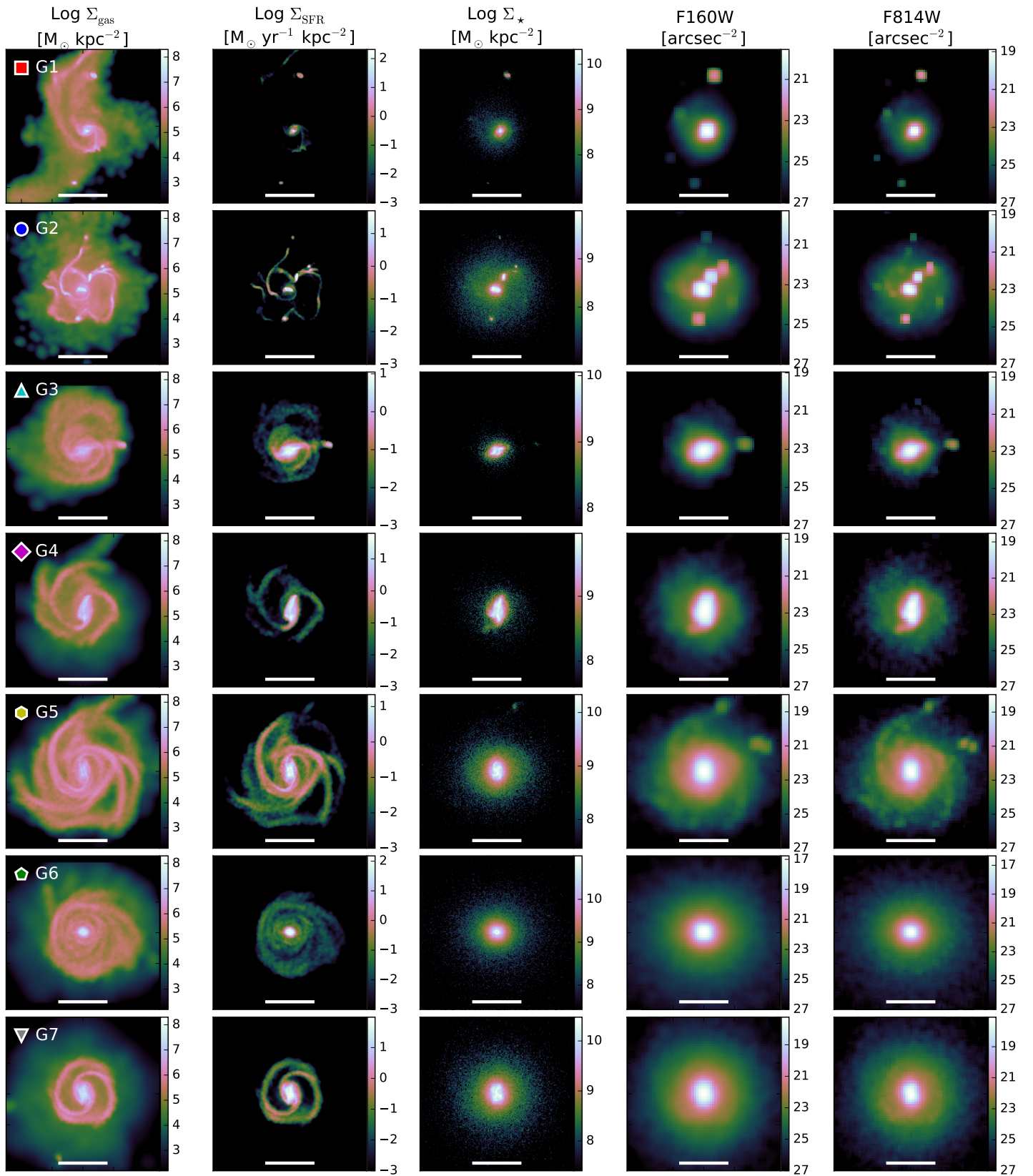


**Figure 3.** Face-on data for each galaxy from Table 1 at  $z=2$ . Columns 1-3 show surface density features, while columns 4 and 5 show each galaxy processed through LOSER in the F160W and F814W bands, respectively, as described in §2.4. The white scale bar corresponds to 5 physical kpc.



dashed line shows the value of  $\mathcal{R} = 0.25$  above which we identify the galaxy as having undergone a major merger since the immediately previous output. From this it is clear that there is hardly any correlation between the concentration parameter and our galaxy sample’s merger state. This is not entirely surprising, as the major merger cut criteria is usually defined in terms of  $A$  (Figure 4). The only significant correlation occurs in the face-on sSFR-weighted fit, but this shows an *anti*-correlation since one expects mergers to increase the concentration.

Figure 6 is constructed in a similar manner to Figure 5 but for the asymmetry parameter. In contrast to the concentration, we find a strong correlation between asymmetry  $A$  and a galaxy’s merger history, with the power-law fits having positive slopes and fairly small errors indicating a highly significant detection of a correlation. However, the scatter around the best fit is still fairly large ( $\sim 0.44$  dex), which means that there is not necessarily a tight correlation between  $\mathcal{R}$  and  $A$ . The correlation appears to be significantly strengthened by a population of high- $\mathcal{R}$  objects that form an upward spur at the highest  $A$  values.

The canonical merger separation value of  $A = 0.35$  (Conselice et al. 2003) is shown as the vertical dashed line, while higher values of  $A = 0.8$  and  $A = 1.5$  are shown as dotted lines that will be investigated in §5. Owing to the large scatter, there are still many galaxies classified as major mergers with asymmetry values  $\geq 0.35$  even though their merger ratios are consistent with minor-mergers or in-situ growth (lower right quadrant). Out of all the data points within this sample, only  $\simeq 9\%$  with  $A \geq 0.35$  are classified correctly as major mergers according to their merger ratios extracted from the simulation.

Two avenues can immediately be seen for potentially improving the fidelity of merger identification using  $A$ . First, it is clear that all but one of the true mergers lie at  $A \gg 0.35$ , hence we can cut at a higher value of  $A$  to obtain a higher fraction of mergers. Second, it is possible that  $A$  identifies mergers well, but perhaps in an earlier phase that is not associated with the final coalescence, or even a later phase. We will investigate these avenues to improve merger characterisation using  $A$  in §5.

### 4.3 *Gini* and $M_{20}$

The *Gini* coefficient originated as an economics statistic representing the income distribution of a nation’s residents. A value of zero means perfect equality, wherein a value of unity represents perfect inequality. When used in galaxy morphology determinations, it quantifies the “lumpiness” of the light distribution, with no prior assumptions about its morphology (Abraham et al. 2003; Lotz et al. 2004). In the context of galaxy images, a *Gini* coefficient of zero means that the flux is evenly distributed among all the pixels, while a value of one means that all of the flux is concentrated in a single pixel.

To compute the *Gini* coefficient we first sort each galaxy’s pixels by flux in increasing order before applying the following equation (e.g. Lotz et al. 2004):

$$Gini = \frac{1}{fn(n-1)} \sum_i^n (2i - n - 1) f_i. \quad (7)$$

Here  $f$  is the flux of each pixel, and  $n$  is the number of pixels in each image.

$M_{20}$  is defined as the normalised second-order moment of the brightest 20% of a galaxy’s flux. This quantity is calculated by again sorting the pixels from highest to lowest flux, then summing over the brightest pixels until reaching 20% of the total flux, and normalising by its total second order moment ( $M_{tot}$ ):

$$M_{20} \equiv \log \left( \frac{\sum_i M_i}{M_{tot}} \right), \text{ while } \sum_i f_i < 0.2 f_{tot}, \quad (8)$$

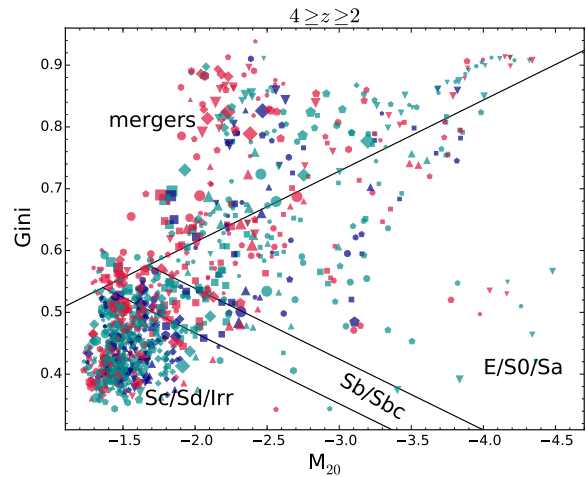


**Figure 7.** *Gini* –  $M_{20}$  relation for our sample of galaxies plotted in the same fashion as Figure 4. The different regions on this plot represent the different morphological classifications that have been applied to local galaxies, and extrapolated to higher redshift observations.

where  $f_{tot}$  is the total flux of the galaxy, and  $f_i$  are the fluxes in each pixel ordered from highest to lowest flux.  $M_{tot}$  is defined as the flux sum of each pixel multiplied by the squared distance to the centre of the galaxy:

$$M_{tot} \equiv \sum_i^n M_i = \sum_i^n f_i [(x_i - x_c)^2 + (y_i - y_c)^2], \quad (9)$$

where  $(x_c, y_c)$  is the galaxy’s centre, and  $(x_i, y_i)$  is the pixel location.

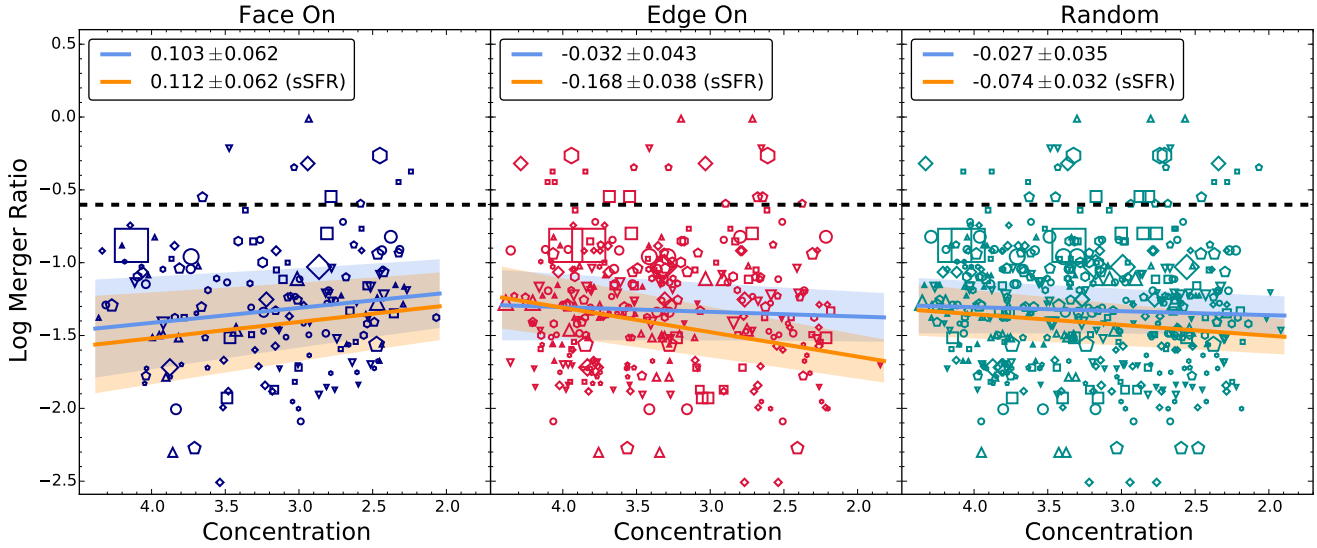
This value encodes similar information as the concentration parameter (§4.2), but differs in two primary aspects: it is more heavily weighted by the spatial distribution of luminous regions because of the  $r^2$  dependence, and it is not measured with circular or elliptical apertures. Lotz et al. (2004) argues that these differences make  $M_{20}$  more sensitive to merger signatures than the concentration parameter.

Akin to  $C$  and  $A$ ,  $G$  and  $M_{20}$  are routinely plotted as a function of one another which we show in Figure 7 for our sample. The different regions on this plot represent the different morphological classifications that have been applied to local galaxies (Lotz et al. 2008). Within our sample, we find a median *Gini* coefficient of 0.51, and a median  $M_{20}$  of -1.74. Hence our typical  $z = 2$  galaxy is an Sb/Sc spiral, which is consistent with the images shown in Figure 3.

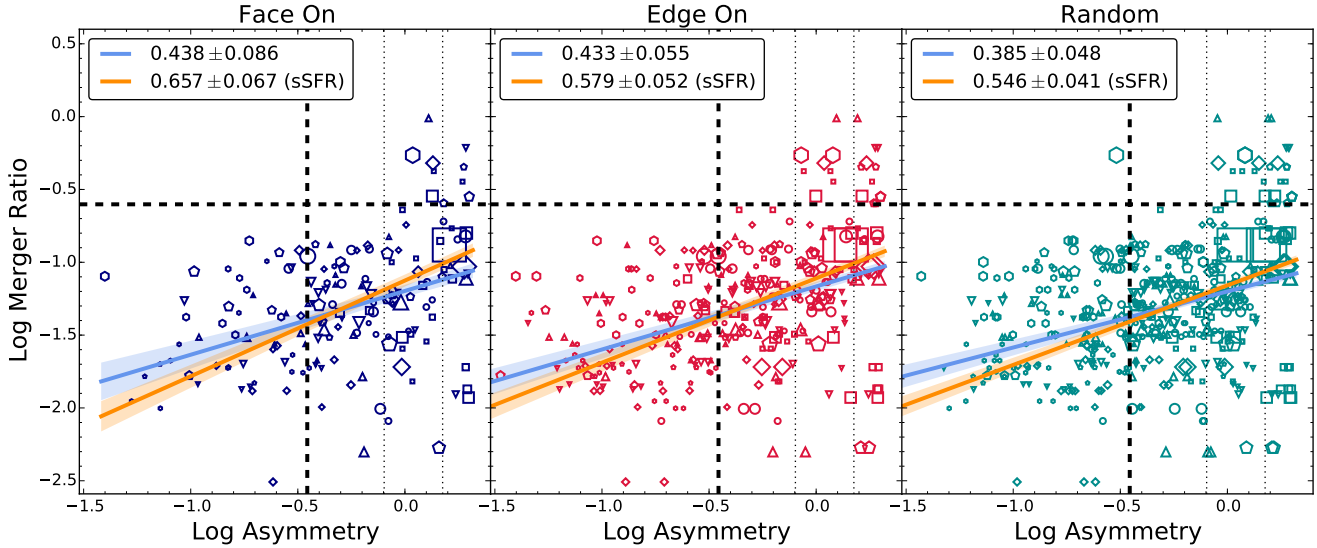
Figure 8 plots the merger ratio ( $\log \mathcal{R}$ ) versus the *Gini* coefficient ( $\log G$ ), similar to Figure 5. By itself, *Gini* is essentially uncorrelated with  $\mathcal{R}$ , except for a weak correlation in the face-on orientation. Not surprisingly, the *Gini* coefficient alone offers a poor way to identify mergers.

Figure 9 plots the merger ratio as a function of the  $M_{20}$  parameter, similar to Figure 5. Again, there is only at most a weak anti-correlation of  $M_{20}$  and merger ratio, and only in the face-on case. Hence both *Gini* and  $M_{20}$  in isolation only can be associated with mergers in the face-on case, and even then not reliably.

We note that Stott et al. (2013) used visual classifications in the HiZELS survey at  $z \sim 0.4$  to calibrate the relationship between *Gini*,  $M_{20}$ , and disturbed morphologies indicative of mergers. They found that a *Gini*-independent cut of  $M_{20} > -1.5$  was efficient at detecting visually-classified mergers. Our results would



**Figure 5.** The merger-ratio  $R$  as a function of the concentration ( $C$ ) parameter discussed in §3.1 split into different panels corresponding to the different viewing angles. Point shapes correspond to different galaxies (see Table 1) while point size corresponds to a galaxy’s sSFR. The dashed line represents the threshold for major mergers with a mass ratio of  $\mathcal{R} = 0.25$ . Two power laws are fit to each panel and shown with  $1\sigma$  error contours; the blue is a result of fitting with no weighting, and the red fit is weighted by the sSFR (§3.5). Legends indicate the power law index with errors.



**Figure 6.** The merger-ratio  $R$  as a function of the asymmetry ( $A$ ), similar to Figure 5. The vertical dashed line represents the canonical asymmetry threshold of  $A \geq 0.35$  (Conselice et al. 2003), while the two dotted vertical lines represent arbitrary thresholds of  $A \geq 0.8$  and 1.5 (§5.2).

not support such a cut being used at  $z \sim 2$ , as it would not do well at identifying galaxies that have just undergone a merger.

#### 4.4 Mergeriness

While Gini and  $M_{20}$  independently do not do well at identifying mergers, typically merger classification relies on a combination of these two parameters. To quantify how well the  $Gini-M_{20}$  relation classifies each data point as a merger, we define the term ‘mergeriness’ as the perpendicular distance to the canonical dividing merger line (similar to what was done in Snyder et al.

2015). A point above this line ( $Gini-M_{20}$  merger) is assigned a positive value, while a point below ( $Gini-M_{20}$  non-merger) is assigned a negative value, given by the distance to the line. The numerical value of this distance in  $Gini-M_{20}$  space has no particular physical interpretation, but can be used as a relative measure to identify how well the  $Gini-M_{20}$  relation classifies mergers.

Figure 10 shows  $\mathcal{R}$  of each object in our sample as a function of mergeriness. Every data point to the left of the vertical dashed line is not classified as a merger on the  $Gini-M_{20}$  plane, while everything to the right is a merger. Each data point above the dashed horizontal line ( $R = -0.46$ ) represents a true major

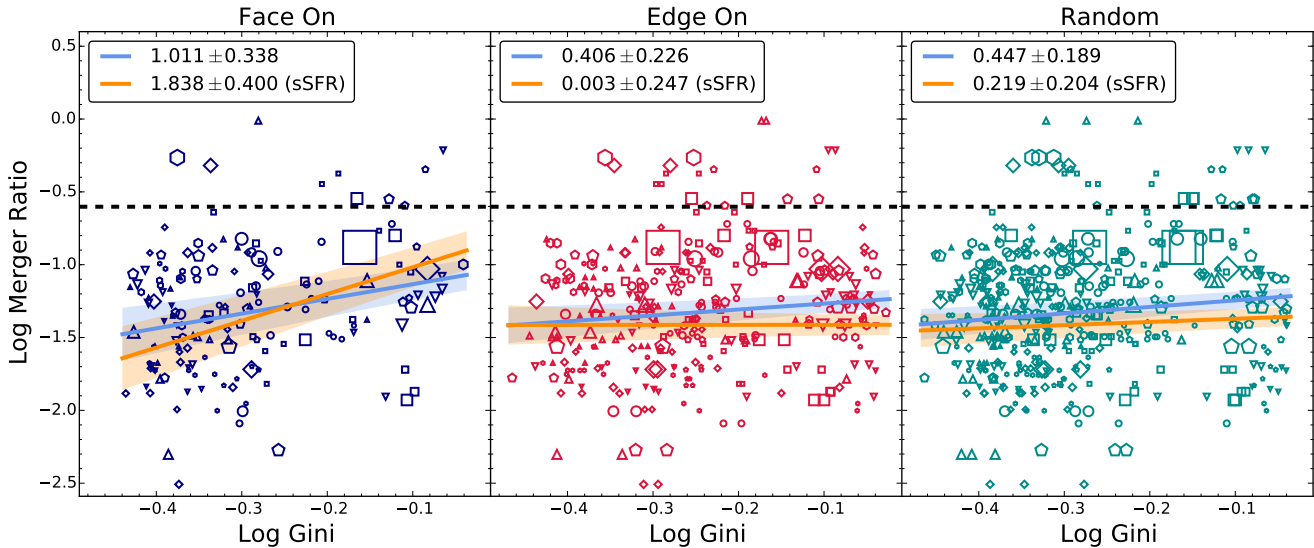


Figure 8. The merger-ratio  $R$  as a function of  $Gini$ , similar to Figure 5.

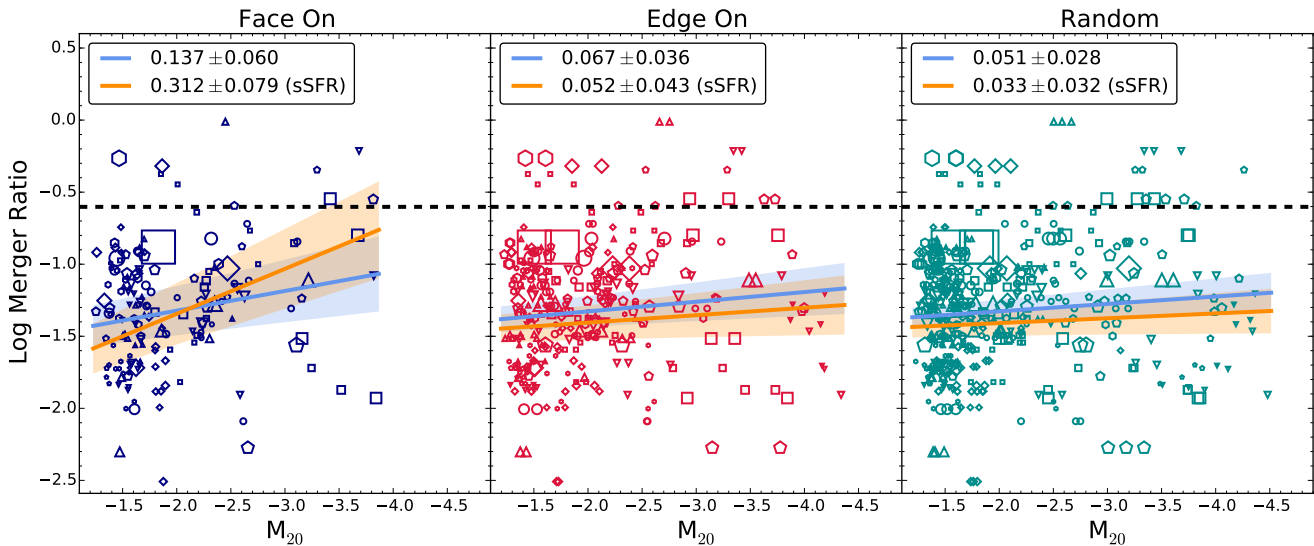


Figure 9. The merger-ratio  $R$  as a function of  $M_{20}$ , similar to Figure 5.

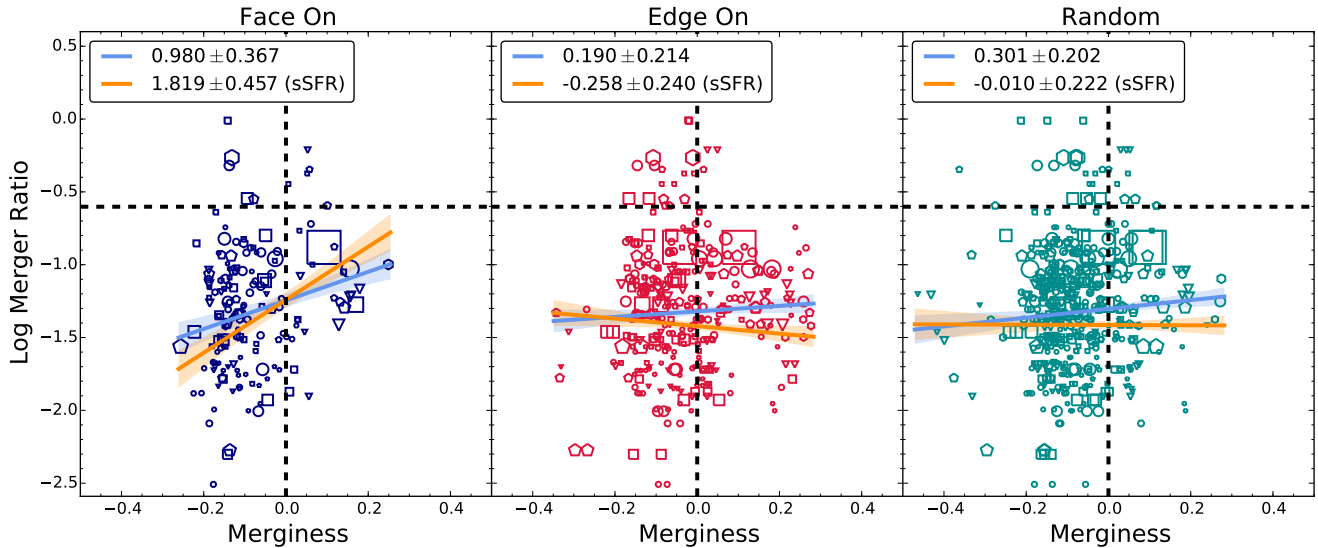
merger (between the previous two outputs) of at least a 1:4 mass ratio. Points in the upper right and lower left quadrants indicate objects that are correctly classified; points in the other two quadrants are incorrectly classified.

Figure 10 indicates that the location in the  $Gini$ - $M_{20}$  relation does not do particularly well at identifying mergers at these redshifts. Points in the upper left quadrant are major mergers in the simulation, yet are classified as non-mergers on the  $Gini$ - $M_{20}$  plane. Points in the lower right on the other hand, have merger ratios consistent with minor-mergers yet are classified as major mergers on the  $Gini$ - $M_{20}$  plane. Out of the 251 data points classified as a merger in the  $Gini$ - $M_{20}$  relation (positive ‘merginess’), only 18 ( $\sim 7\%$ ) lie above the  $R > 0.25$  line and are a direct result of major mergers.

Fits to the data suggest very little correlation, with the exception of face-on galaxies that have a power-law slope that deviates by more than  $3\sigma$  from zero. This correlation is still much

less significant than for the asymmetry ( $A$ ). In particular, unlike for  $A$  where many of the true mergers lie at high- $A$ , here the true mergers are not well-localised in merginess. Even for the face-on case, there are only 5 major mergers out of the 31 with positive merginess ( $\sim 16\%$ ) that are correctly classified.

In summary, of the non-parametric morphological statistics examined here, only asymmetry provides a clear correlation with mergers, with the  $Gini$ - $M_{20}$ -based merginess parameter showing some correlation only in the case of face-on galaxies. Recall, however, that our merger quantification only picks out major mergers that have occurred between the previous two outputs. It is possible, as was mentioned for asymmetry, that these statistics might not identify mergers exactly when they end, but perhaps they do better at identifying recent or future mergers. We examine this in the next section.



**Figure 10.** The merger-ratio  $R$  as a function of the merginess, similar to Figure 5. We additionally plot a vertical dotted line at merginess= 0 to differentiate between a merger (positive merginess) and a non-merger (negative merginess) on the  $Gini - M_{20}$  plane.

## 5 MORPHOLOGICAL STATISTICS IN TIME

In this section we plot each morphological statistic and merger ratio over varying intervals in cosmic time. First, we qualitatively examine the evolution of each of our statistics, in relation to the evolution of the merger ratio. Then, we quantify how well each statistic does at tracking mergers over a range of time intervals. For brevity, we omit consideration of Gini and  $M_{20}$  individually, and focus only on the merginess parameter defined by the location in  $Gini-M_{20}$  space.

### 5.1 Evolution of statistics

In the figures of this section, we overlay the evolution of the merger ratio  $\mathcal{R}$  and each morphological statistic from  $4 \geq z \geq 2$ . We consider separately the three cases of face-on, edge-on, and random orientations; for the two cases with multiple data points (edge-on and random) we take the median value at any given redshift. We plot the merger ratio  $\mathcal{R}$  as a dashed line and plot the dividing line between major and minor mergers as a horizontal dotted line; hence major mergers are when the dashed line goes above the dotted line.

Figure 11 shows the concentration of each of our seven galaxies in various orientations as a function of cosmic time. We see that there is no indication that  $C$  is strongly impacted by major mergers, in accord with our findings in §4.2. In some instances the concentration parameter will spike shortly before or after a major merger, but overall there is no consistent correlation between a high  $\mathcal{R}$  and  $C$ . This is not surprising since  $C$  is not typically used to classify mergers.

Figure 12 similarly shows the asymmetry  $A$  as a function of time, with  $\mathcal{R}$  overlaid as before. Here we immediately notice that in many cases, spikes in  $A$  mimic spikes in  $\mathcal{R}$ . The correlation is certainly not tight, but it does appear that overall when  $\mathcal{R}$  is large,  $A$  is often large as well. Again, this reflects the results we obtained in §4.2, but with the additional information that there is a more general temporal correlation between these quantities.

We argued that a higher cut than the canonical  $A \geq 0.35$  (indicated by the horizontal dot-dashed line; Conselice et al. 2003) may be more effective at identifying mergers. This is also evident in this plot, but the optimal cut is not obvious; each galaxy would

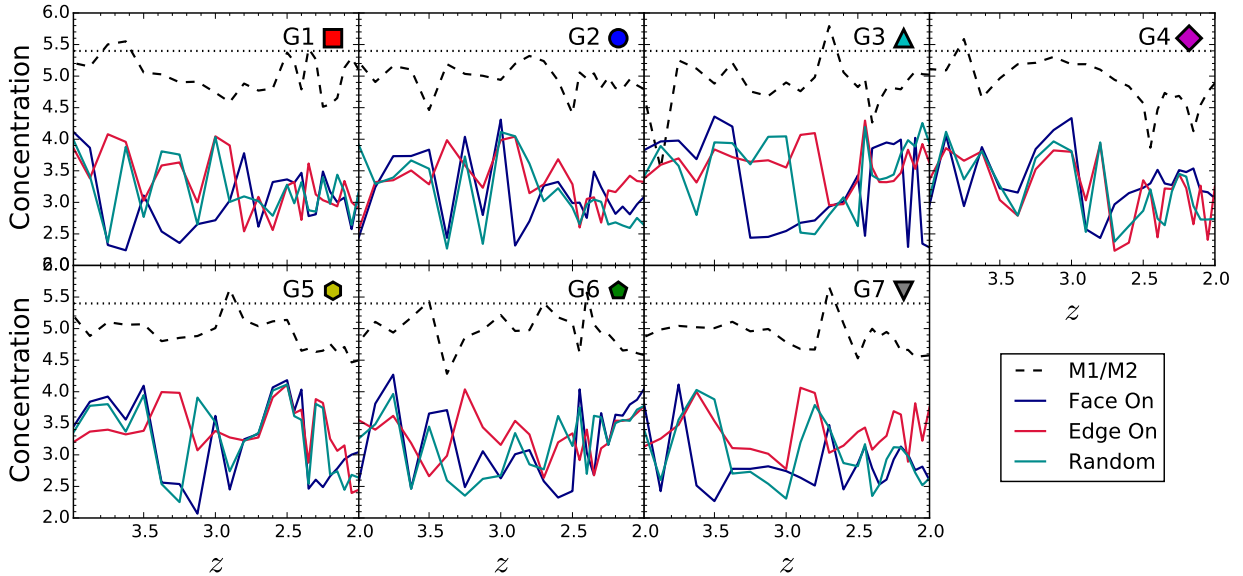
require a different cut in  $A$  to allow for a complete selection of major mergers. For G1, G3, G4, G6, and G7 for instance, a cut around  $A \gtrsim 2$  would identify mergers well. But this cut would not work for G2 since it never encounters a major merger yet the asymmetry approaches two at  $z \sim 2.7$ . For G5, conversely, its asymmetry history stays below the Conselice et al. (2003)  $A \geq 0.35$  cut until the major merger event, at which point  $A$  exceeds 0.35 and remains above the cut for  $\sim 3$  outputs after the major merger. This particular galaxy has a similarly smooth growth history similar to G2, yet its asymmetry history is much calmer. G5 is the galaxy within our sample showing the most well-settled disk-like morphology at  $z = 2$  akin to low-redshift galaxies, which may help to explain why a cut of  $A \geq 0.35$  can correctly identify the major merger for this galaxy alone.

Figure 13 analogously shows the merginess as a function of cosmic time for the galaxies in our sample. It is clear that the actual merger event does not straightforwardly increase the merginess, as we saw in §4.4. On occasion, however, the merginess spikes at a time that is close to, but not exactly coincident with, the merger event. We will quantify this in the next section.

### 5.2 A quantitative assessment of $A$ and merginess in time

We now ask the question, do  $A$  and merginess identify mergers that have happened within a certain time interval from the time of observation? In other words, if one observes a galaxy at a given redshift to have a high value of  $A$  or merginess, what is the probability that it recently underwent or will soon complete a merger?

To quantify this, we re-assign the values of  $\mathcal{R}$  around our ten major merger events for  $\pm N$  surrounding time steps to the  $\mathcal{R}$  at the time of the major merger itself. This equates to adjusting the  $y$ -axis values in Figures 6 and 10 for data points  $\pm N$  time steps around each major merger, guaranteeing that these data points will be considered a major merger according to their merger ratios. We can then measure the fraction of objects above a given asymmetry or merginess threshold that also have a  $\mathcal{R}$  consistent with a major merger. In this way, we can quantitatively answer the question, does a high value of  $A$  or merginess correspond to identifying a merger within some time interval  $\Delta t$  (corresponding to  $\pm N$  outputs)?



**Figure 11.** The concentration parameter  $C$  as a function of cosmic time for our seven galaxies. We consolidate our 6 viewing angles into either face-on, edge-on, or random; because the latter two have multiple data points we take the median values. We also show the normalised merger-ratio history of each galaxy as the dashed line, with the dotted line representing the threshold for a major merger; a major merger occurs when the dashed line crosses above this dotted line.

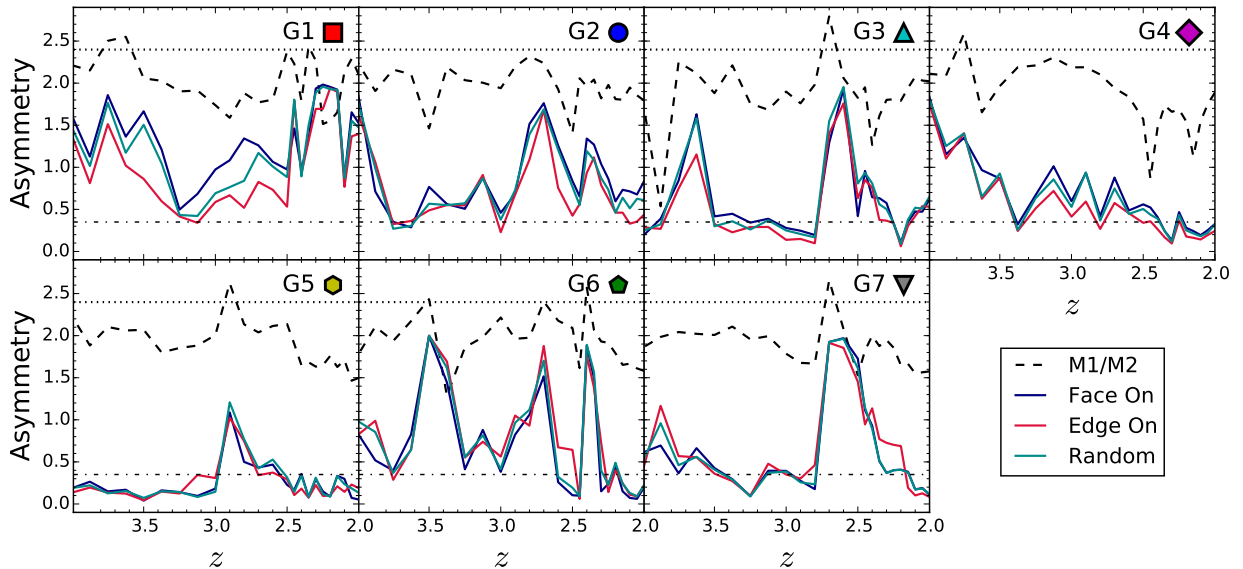


**Figure 12.** The asymmetry parameter  $A$  as a function of cosmic time for our seven galaxies, similar to Figure 11. Asymmetry values above  $A \geq 0.35$  are canonically considered major mergers (Conselice et al. 2003); we plot this threshold as a dot-dashed line.

Figure 14 shows these fractions for various thresholds of  $A$  for our different viewing orientations, as a function of the time interval  $\pm\Delta t$ . The solid lines represent the fraction of correctly identified major mergers for a given  $\Delta t$  with  $A \geq 0.35$  (Conselice et al. 2003), while the dashed and dotted lines show  $A \geq 0.8$  and  $A \geq 1.5$ , respectively. The dot-dashed line considers all values of  $A$  (i.e.  $A > 0$ ), so effectively shows the “background noise” that signifies the likelihood of being within  $\pm\Delta t$  of a merger at any given time. Error bars for the random viewing orientation

represent the spread in the fraction of correctly identified mergers for the  $x$ ,  $y$ , and  $z$  viewing orientations independently.

We can see that a galaxy within our sample having  $A \geq 0.35$  provides little better merger identification than the noise, for any time interval and viewing orientation. However, increasing the cut to  $A \geq 0.8$  significantly increases the ability to identify mergers. A galaxy satisfying this cut has a  $\sim 50\%$  chance of being within  $\pm 200$  Myr of a merger.  $A \geq 1.5$  provides even higher percentages, so that there is now a  $\sim 70\%$  chance of a major merger

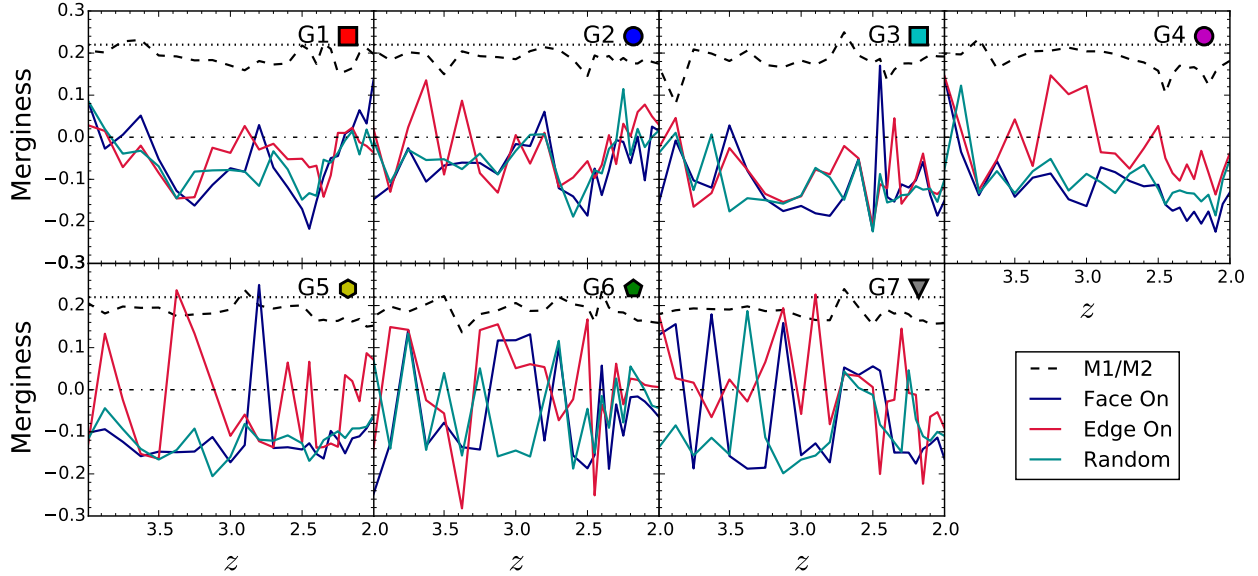


**Figure 13.** The ‘merginess’ as a function of cosmic time for our seven galaxies, similar to Figure 11. The dot-dashed line represents the difference between a merger (positive merginess) and a non-merger (negative merginess) in the  $Gini - M_{20}$  plane.

within  $\pm 0.2$  Gyr. The percentages are somewhat higher for edge-on systems than face-on, indicating that  $A$  is better at identifying mergers in edge-on systems.

There is also the converse question, i.e. what fraction of true mergers are identified as such by these cuts? For  $A \geq 0.35$ , it finds all but one of the true mergers (while also unfortunately finding many that are not).  $A \geq 0.8$  identifies 90% (9/10) of all major mergers, while  $A \geq 1.5$  identifies only 60% (6/10) of them. Hence, while an increased cut improves the accuracy of merger identification, it sacrifices the ability to identify a highly complete sample of merger events.

Figure 15 shows the analogous fractions of correctly-identified mergers for various merginess thresholds, as a function of  $\pm \Delta t$ . For the random orientation case, merginess provides essentially no benefit for identifying mergers relative to the background noise. Only in the face-on case does merginess provide additional information regarding a merger, and interestingly only for  $\Delta t \gtrsim 200$  Myr. Changing the merginess cut does little to help, unlike in the asymmetry case where a more stringent cut greatly improves the fidelity of merger identification.

So far we have considered intervals symmetric in time, i.e. we have not distinguished whether a given statistic better identifies pre-mergers or merger remnants. Figure 16 shows the effectiveness of merger identification for  $A$  considering positive and negative  $\Delta t$  separately. It is clear that  $A$  preferentially identifies pre-coalescence mergers, and shows the same slight preference for identifying these in edge-on systems as before.

Merginess, on the other hand, displays a minor preference for identifying merger remnants in the face-on case, as illustrated in Figure 17, but edge-on and random viewing orientations still provide little to no benefit compared to the background noise. Increasing the merginess threshold typically yields a decrease in the fraction of correctly identified mergers when looking in the  $-\Delta t$  direction. In the  $+\Delta t$  direction, however, we find that increases in the merginess threshold provides minor benefits only at  $\Delta t \gtrsim 200$  Myr.

In short, a high value in the asymmetry ( $A$ ), such as 0.8, provides the best way to identify major mergers at  $z \sim 2 - 4$ . It fares slightly better in the edge-on systems than in face-on ones,

but even for a random orientation a galaxy with  $A \geq 0.8$  has a  $\approx 50\%$  chance of being involved in a merger within  $\pm 0.2$  Gyr, and it identifies all but one merger in our sample. A higher cut of  $A > 1.5$  provides a greater probability for being (temporally) close to a merger, at the cost of a significantly incomplete sample of mergers. The location in the  $Gini - M_{20}$  plane, as quantified by ‘merginess’, is only mildly effective at identifying mergers in the face-on case, and ineffective in the edge-on or random orientations. Moreover, no other cut in merginess is significantly more effective. We thus conclude that asymmetry represents a better, though not perfect, approach to identifying mergers in high- $z$  galaxies than  $Gini - M_{20}$ .

### 5.3 Resolution dependence

To assess the resolution dependence of our results, we examine the lower-resolution counterparts to the galaxies listed in Table 1 from the original low-resolution full box simulation (§2.2). By subtracting the fractional value from the background noise (§5.2) we can quantify the increase in the fraction of mergers correctly identified in relation to the background noise for each of our  $A$  and merginess cuts.

Figures 18 and 19 show this fractional increase with respect to the background noise for the random viewing orientation (we omit the face-on and edge-on viewing orientations as they show similar trends). The left panels show the results for the low-resolution galaxy sample, while the right panels shows the high-resolution zoom sample. As in Figures 14-17, the error bars represent the spread in the percentage increase in the fraction of correctly identified mergers when examining the  $x$ ,  $y$ , and  $z$  viewing orientations independently.

We find that the general conclusions drawn here as regards the efficacy of  $A$  and merginess are not overly sensitive to resolution. We do find that the overall fraction of correctly identified systems along with the background noise level both increase somewhat with a decrease in resolution, but the difference between the two remains similar.

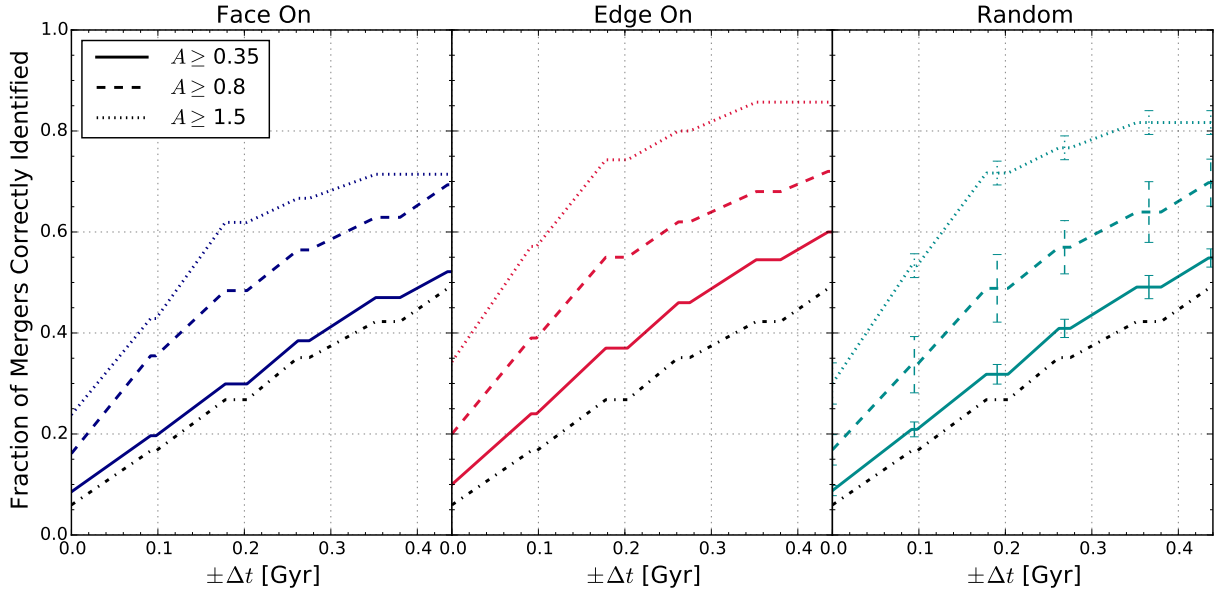


**Figure 14.** The fraction of major mergers correctly identified above a given asymmetry threshold when we consider the time dependent effects discussed in §5.2. The solid lines represent the typical asymmetry cut ( $A \geq 0.35$ ; Conselice et al. 2003) used to identify major merger candidates, while higher cuts of 0.8 (dashed) and 1.5 (dotted) are arbitrary choices to illustrate the effectiveness of  $A$  at selecting major mergers within our sample. The black dot-dashed line is the chance of encountering a random merger over a given  $\pm\Delta t$  as if there were no threshold value (background noise). Error bars represent the spread in the fraction mergers correctly identified when examining the  $x$ ,  $y$ , and  $z$  viewing orientations independently.

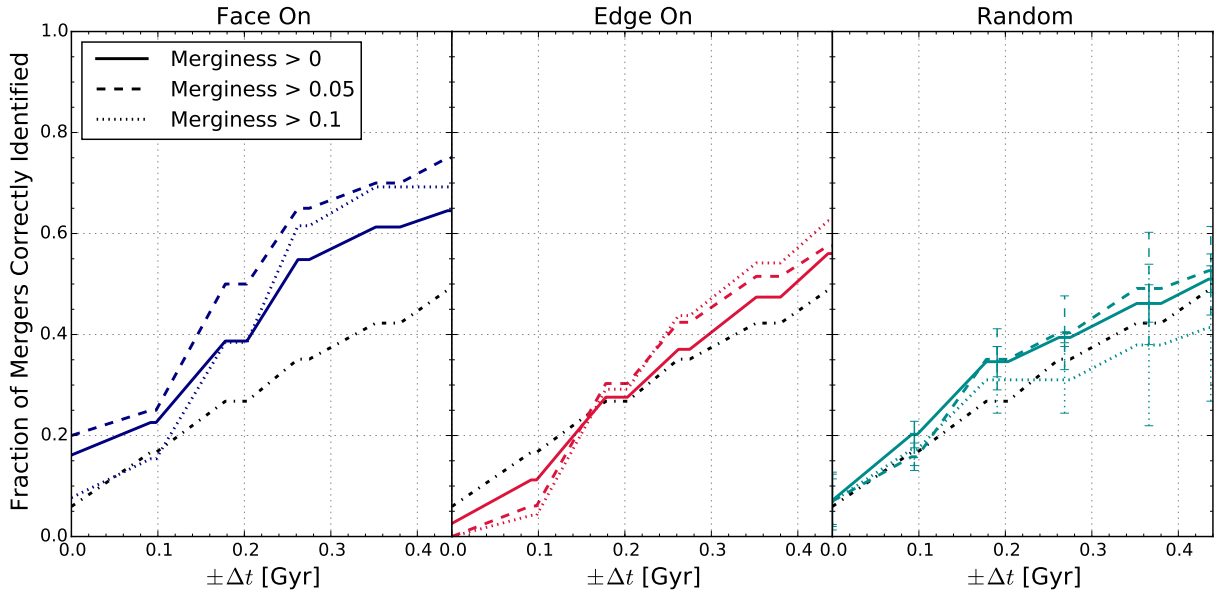


**Figure 15.** The fraction of major mergers correctly identified above a given merginess threshold when we consider the time dependent effects discussed in §5.2. The solid lines represents a merginess threshold of merginess=0 used to identify major merger candidates on the  $Gini-M_{20}$  plane, while higher thresholds of 0.05 (dashed) and 0.1 (dotted) are arbitrary choices to illustrate the effect of shifting the merginess threshold. The black dot-dashed line is the chance of encountering a random merger over a given  $\pm\Delta t$  as if there were no merginess threshold (background noise). Error bars represent the spread in the fraction mergers correctly identified when examining the  $x$ ,  $y$ , and  $z$  viewing orientations independently.

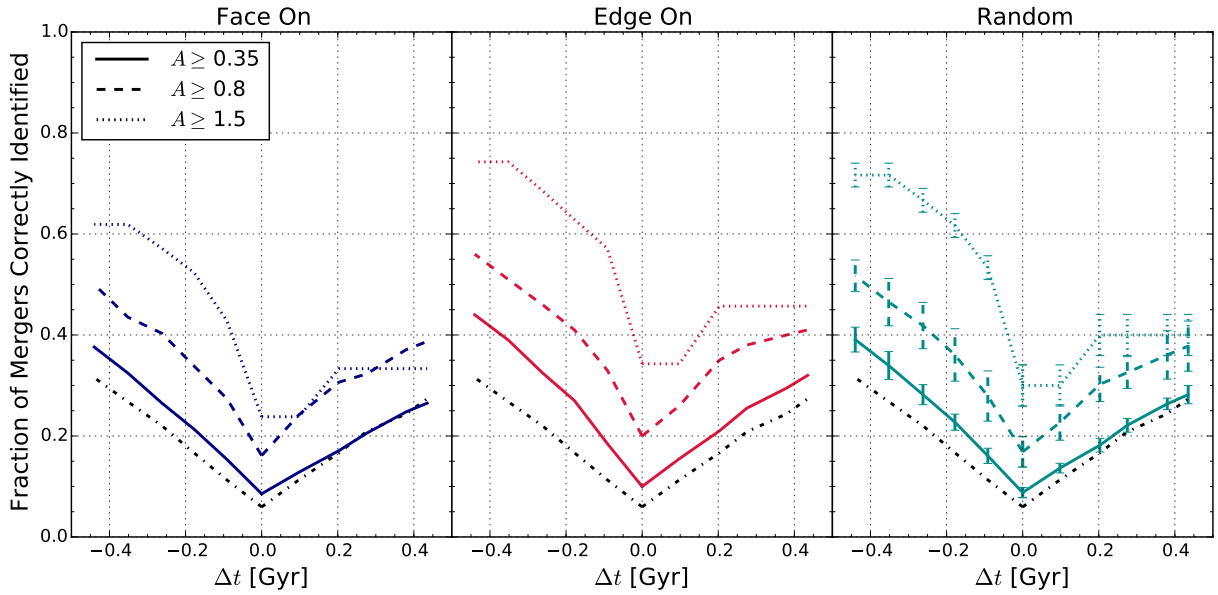


**Figure 16.** Similar to Figure 14, but here we plot the fraction of mergers correctly identified when separately considering the  $+\Delta t$  and  $-\Delta t$  time dependent effects discussed in §5.2 for the asymmetry parameter.

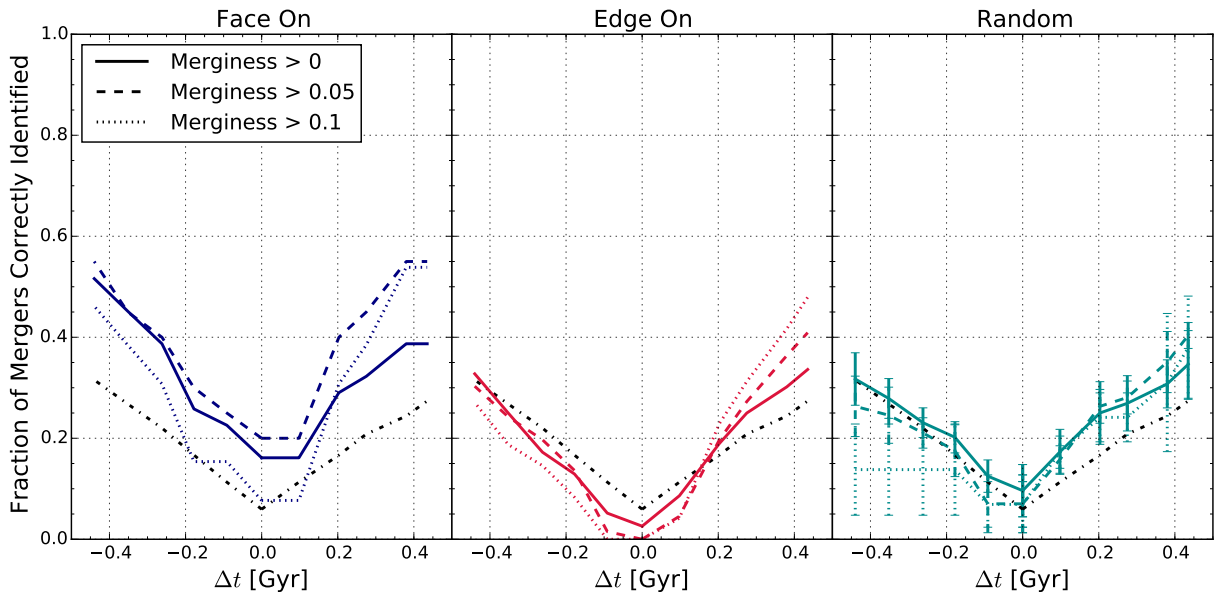


**Figure 17.** Similar to Figure 15, but here we plot the fraction of mergers correctly identified when separately considering the  $+\Delta t$  and  $-\Delta t$  time dependent effects discussed in §5.2 for the mergeriness parameter.

## 6 CONCLUSIONS

We have performed high-resolution cosmological zoom-in simulations to investigate the evolution of nonparametric galaxy morphological statistics and their relationship to major mergers at  $z \geq 2$ . We consider 7 galaxies with  $3.5 \times 10^9 < M_* < 6.6 \times 10^{10} M_\odot$  and  $2 \times 10^{11} < M_{\text{halo}} < 10^{12} M_\odot$  at  $z = 2$  having star formation rates from  $5 - 60 M_\odot \text{yr}^{-1}$ . By post-processing our simulated galaxies through LOSER, we create mock images of each object as if it were observed with *HST* WFC3’s F160W filter. The fluxes from our simulated images are used to calculate the concentration

( $C$ ), asymmetry ( $A$ ), *Gini* coefficient ( $G$ ), and the normalised second-order moment of the brightest 20% of a galaxy’s flux ( $M_{20}$ ). We track the mass growth history of each galaxy from  $4 \geq z \geq 2$  and identify 10 major merger events of at least a 1:4 mass-ratio, and search for correlations with the above mentioned morphological statistics that could most reliably identify such merger events.

Our main findings are as follows:

- The asymmetry statistic ( $A$ ) strongly correlates with merger ratio among our simulated galaxies at these redshifts (Figures 6 and 12). Concentration, *Gini*, and  $M_{20}$  do not substantially cor-



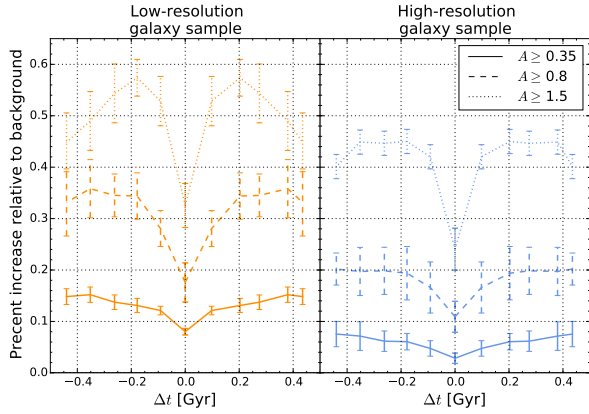


**Figure 18.** Fractional increase in the fraction of correctly identified major mergers when compared to the background noise (§5.2) for three cuts in  $A$  and random viewing orientation. *Left:* results from the low-resolution galaxy sample (§2.2), *Right:* results from the high-resolution zoom sample used throughout this work. Error bars represent the spread in the increase in the fraction of correctly identified mergers when examining the  $x$ ,  $y$ , and  $z$  viewing orientations independently.

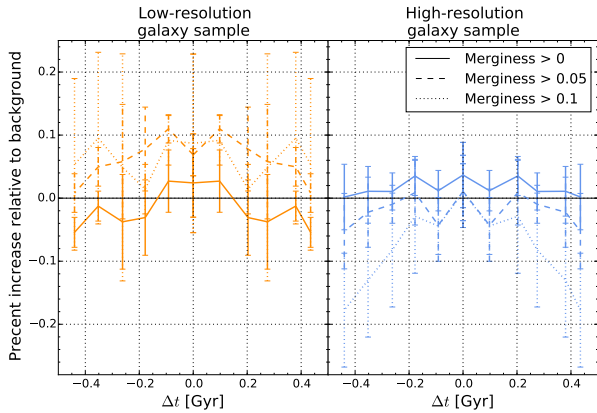


**Figure 19.** Similar to Figure 18 for the merginess parameter.

relate with merger ratio. We define a ‘merginess’ parameter that quantifies the distance from the merger dividing line in  $Gini-M_{20}$  space, but this also does not correlate with merger ratio, except for a weak correlation in the face-on case (§4.4).

- Examining  $A$  in more detail, we find that a higher threshold for  $A$  than the canonically-used 0.35 provides a more robust identification of mergers. For instance  $A \geq 0.8$  identifies 9/10 of our mergers, with a much lower fraction of erroneously-identified mergers,  $\sim 50\%$ .  $A \geq 1.5$  further reduces erroneous identifications, but only identifies about half the mergers in our sample.

- We examine the temporal dependence of these parameters by quantifying how well each statistic identifies a merger that is about to happen or has just happened within some time  $\Delta t$  (§5.2). The merginess parameter (from  $Gini-M_{20}$ ) only weakly identifies mergers above random sampling in the face-on case, but does not properly identify mergers in the random orientation case. (Figure 8).

- The probability of  $A$  correctly identifying a merger increases with both  $\Delta t$  and the threshold value. A galaxy with  $A \geq 0.8$  has a  $\sim 50\%$  chance of being an object that experiences a merger within  $\pm 200$  Myr. The probability increases to  $\sim 70\%$  for  $A \geq 1.5$ ,

at the cost of a less complete sample of mergers. (Figure 14).  $A$  also preferentially identifies pre-coalescence mergers (Figure 16).

- Within our sample, compact galaxies (as defined by Barro et al. 2013) are formed naturally via in-situ growth or minor-mergers. In some instances major mergers can briefly force a galaxy to become compact, after a period where galaxies become more extended as measured by their half-light radius.

Overall, we find that the best approach for identifying mergers from  $z = 2$  to 4 is to use the asymmetry statistic ( $A$ ) with a higher cut than used for low- $z$  galaxies. With larger samples we will be able to quantify these statistics in more detail, and in future work we will also examine the sensitivity to numerical methodologies in greater detail. It is also possible that resolved colour maps may provide additional information regarding the evolutionary state of galaxies. It is hoped that these types of investigations will aid the interpretation of resolved studies of high-redshift galaxies that have emerged using *HST* and will be significantly furthered in the *JWST* era.

## ACKNOWLEDGEMENTS

Analysis performed with pyGadgetReader (Thompson 2014) and SPHGR (Thompson 2015). Simulations were run on the University of Arizona’s El Gato supercomputer<sup>4</sup> funded by NSF MRI grant 1228509, and the University of the Western Cape’s Timon and Pumbaa clusters. This work was supported by NASA grant NNX12AH86G. RD and RT acknowledge support from the South African Research Chairs Initiative and the South African National Research Foundation. This publication is funded in part by the Gordon and Betty Moore Foundation’s Data-Driven Discovery Initiative through Grant GBMF4561. The authors thank J. Lotz, G. Snyder, and R. Somerville for helpful discussions.

## REFERENCES

- Abraham, R. G., van den Bergh, S., Glazebrook, K., Ellis, R. S., Santiago, B. X., Surma, P., & Griffiths, R. E. 1996, *ApJS*, 107, 1
- Abraham, R. G., van den Bergh, S., & Nair, P. 2003, *ApJ*, 588, 218
- Balsara, D. S. 1989, PhD thesis, Univ. Illinois at Urbana-Champaign, (1989)
- Barro, G., Faber, S. M., Pérez-González, P. G., Koo, D. C., Williams, C. C., Kocevski, D. D., Trump, J. R., Mozena, et al. 2013, *ApJ*, 765, 104
- Behroozi, P. S., Wechsler, R. H., & Wu, H.-Y. 2013, *ApJ*, 762, 109
- Bershady, M. A., Jangren, A., & Conselice, C. J. 2000, *AJ*, 119, 2645
- Brinchmann, J., Abraham, R., Schade, D., Tresse, L., Ellis, R. S., Lilly, S., Le Fèvre, O., Glazebrook, K., Hammer, F., Colless, M., Crampton, D., & Broadhurst, T. 1998, *ApJ*, 499, 112
- Brooks, A. M., Solomon, A. R., Governato, F., McCleary, J., MacArthur, L. A., Brook, C. B. A., Jonsson, P., Quinn, T. R., & Wadsley, J. 2011, *ApJ*, 728, 51
- Bruce, V. A., Dunlop, J. S., Cirasuolo, M., McLure, R. J., Targett, T. A., Bell, E. F., Croton, D. J., Dekel, A., Faber, S. M., Ferguson, H. C., Grogin, N. A., Kocevski, D. D., Koekemoer, A. M., Koo, D. C., Lai, K., Lotz, J. M., McGrath, E. J., Newman, J. A., & van der Wel, A. 2012, *MNRAS*, 427, 1666
- Calzetti, D., Armus, L., Bohlin, R. C., Kinney, A. L., Koornneef, J., & Storchi-Bergmann, T. 2000, *ApJ*, 533, 682

<sup>4</sup> <http://elgato.arizona.edu/>

- Cassata, P., Cimatti, A., Franceschini, A., Daddi, E., Pignatelli, E., Fasano, G., Rodighiero, G., Pozzetti, L., Mignoli, M., & Renzini, A. 2005, *MNRAS*, 357, 903
- Cibinel, A., Le Floch, E., Perret, V., Bournaud, F., Daddi, E., Pannella, M., Elbaz, D., Amram, P., & Duc, P.-A. 2015, *ApJ*, 805, 181
- Conroy, C. & Gunn, J. E. 2010, *ApJ*, 712, 833
- Conroy, C., Gunn, J. E., & White, M. 2009, *ApJ*, 699, 486
- Conselice, C. J. 2014, *ARA&A*, 52, 291
- Conselice, C. J., Bershady, M. A., Dickinson, M., & Papovich, C. 2003, *AJ*, 126, 1183
- Conselice, C. J., Bershady, M. A., & Jangren, A. 2000, *ApJ*, 529, 886
- Conselice, C. J., Rajgor, S., & Myers, R. 2008, *MNRAS*, 386, 909
- Cox, T. J., Jonsson, P., Somerville, R. S., Primack, J. R., & Dekel, A. 2008, *MNRAS*, 384, 386
- Croton, D. J., Springel, V., White, S. D. M., De Lucia, G., Frenk, C. S., Gao, L., Jenkins, A., Kauffmann, G., Navarro, J. F., & Yoshida, N. 2006, *MNRAS*, 365, 11
- Daddi, E., Alexander, D. M., Dickinson, M., Gilli, R., Renzini, A., Elbaz, D., Cimatti, A., Chary, R., Frayer, D., Bauer, F. E., Brandt, W. N., Giavalisco, M., Grogin, N. A., Huynh, M., Kurk, J., Mignoli, M., Morrison, G., Pope, A., & Ravindranath, S. 2007, *ApJ*, 670, 173
- Davé, R. 2008, *MNRAS*, 385, 147
- Davé, R., Finlator, K., & Oppenheimer, B. D. 2011, *MNRAS*, 416, 1354
- Davé, R., Katz, N., Oppenheimer, B. D., Kollmeier, J. A., & Weinberg, D. H. 2013, *MNRAS*, 434, 2645
- De Cia, A., Ledoux, C., Savaglio, S., Schady, P., & Vreeswijk, P. M. 2013, *A&A*, 560, A88
- de Vaucouleurs, G. 1948, *Annales d'Astrophysique*, 11, 247
- Dekel, A., Sari, R., & Ceverino, D. 2009, *ApJ*, 703, 785
- Duncan, K., Conselice, C. J., Mortlock, A., Hartley, W. G., Guo, Y., Ferguson, H. C., Davé, R., Lu, Y., Ownsworth, J., Ashby, M. L. N., Dekel, A., Dickinson, M., Faber, S., Giavalisco, M., Grogin, N., Kocevski, D., Koekemoer, A., Somerville, R. S., & White, C. E. 2014, *MNRAS*, 444, 2960
- Durier, F. & Dalla Vecchia, C. 2012, *MNRAS*, 419, 465
- Elmegreen, B. G., Elmegreen, D. M., Fernandez, M. X., & Lomonias, J. J. 2009, *ApJ*, 692, 12
- Erb, D. K., Steidel, C. C., Shapley, A. E., Pettini, M., Reddy, N. A., & Adelberger, K. L. 2006, *ApJ*, 646, 107
- Fang, G., Ma, Z., Kong, X., & Fan, L. 2015, *ApJ*, 807, 139
- Feldmann, R. & Mayer, L. 2015, *MNRAS*, 446, 1939
- Finlator, K., Davé, R., Papovich, C., & Hernquist, L. 2006, *ApJ*, 639, 672
- Ford, A. B., Werk, J. K., Dave, R., Tumlinson, J., Bordoloi, R., Katz, N., Kollmeier, J. A., Oppenheimer, B. D., Peeples, M. S., Prochaska, J. X., & Weinberg, D. H. 2015, *ArXiv e-prints:1503.02084*
- Förster Schreiber, N. M., Genzel, R., Bouché, N., Cresci, G., Davies, R., Buschkamp, P., Shapiro, K., Tacconi, L. J., et al. 2009, *ApJ*, 706, 1364
- Gabor, J. M. & Bournaud, F. 2014, *MNRAS*, 441, 1615
- Gabor, J. M., Davé, R., Finlator, K., & Oppenheimer, B. D. 2010, *MNRAS*, 407, 749
- Genzel, R., Newman, S., Jones, T., Förster Schreiber, N. M., Shapiro, K., Genel, S., Lilly, S. J., Renzini, et al. 2011, *ApJ*, 733, 101
- Governato, F., Moore, B., Cen, R., Stadel, J., Lake, G., & Quinn, T. 1997, *NewA*, 2, 91
- Governato, F., Willman, B., Mayer, L., Brooks, A., Stinson, G., Valenzuela, O., Wadsley, J., & Quinn, T. 2007, *MNRAS*, 374, 1479
- Graham, A. W., Dullo, B. T., & Savorgnan, G. A. D. 2015, *ApJ*, 804, 32
- Grogin, N. A., Kocevski, D. D., Faber, S. M., Ferguson, H. C., Koekemoer, A. M., Riess, A. G., Acquaviva, V., Alexander, et al. 2011, *ApJS*, 197, 35
- Hahn, O. & Abel, T. 2011, *MNRAS*, 415, 2101
- Hopkins, P. F. 2013, *MNRAS*, 428, 2840
- Huang, S. et al. 2015, In prep.
- Jonsson, P. 2006, *MNRAS*, 372, 2
- Katz, N. & Gunn, J. E. 1991, *ApJ*, 377, 365
- Katz, N., Weinberg, D. H., & Hernquist, L. 1996, *ApJS*, 105, 19
- Kennicutt, Jr., R. C. 1998, *ApJ*, 498, 541
- Kereš, D., Katz, N., Weinberg, D. H., & Davé, R. 2005, *MNRAS*, 363, 2
- Koekemoer, A. M., Faber, S. M., Ferguson, H. C., Grogin, N. A., Kocevski, D. D., Koo, D. C., Lai, K., Lotz, J. M., et al. 2011, *ApJS*, 197, 36
- Koekemoer, A. M., Fruchter, A. S., Hook, R. N., & Hack, W. 2003, in *HST Calibration Workshop : Hubble after the Installation of the ACS and the NICMOS Cooling System*, ed. S. Arribas, A. Koekemoer, & B. Whitmore, 337
- Krumholz, M. R., Dekel, A., & McKee, C. F. 2012, *ApJ*, 745, 69
- Krumholz, M. R., McKee, C. F., & Tumlinson, J. 2008, *ApJ*, 689, 865
- . 2009, *ApJ*, 693, 216
- Krumholz, M. R. & Tan, J. C. 2007, *ApJ*, 654, 304
- Lada, C. J., Lombardi, M., & Alves, J. F. 2010, *ApJ*, 724, 687
- Law, D. R., Shapley, A. E., Steidel, C. C., Reddy, N. A., Christensen, C. R., & Erb, D. K. 2012, *Nature*, 487, 338
- Lotz, J. M., Davis, M., Faber, S. M., Guhathakurta, P., Gwyn, S., Huang, J., Koo, D. C., Le Floch, E., Lin, L., Newman, J., Noeske, K., Papovich, C., Willmer, C. N. A., Coil, A., Conselice, C. J., Cooper, M., Hopkins, A. M., Metevier, A., Primack, J., Rieke, G., & Weiner, B. J. 2008, *ApJ*, 672, 177
- Lotz, J. M., Jonsson, P., Cox, T. J., & Primack, J. R. 2010a, *MNRAS*, 404, 590
- . 2010b, *MNRAS*, 404, 575
- Lotz, J. M., Primack, J., & Madau, P. 2004, *AJ*, 128, 163
- Lu, Z., Mo, H. J., Lu, Y., Katz, N., Weinberg, M. D., van den Bosch, F. C., & Yang, X. 2014, *MNRAS*, 439, 1294
- . 2015, *MNRAS*, 450, 1604
- Madau, P. 1995, *ApJ*, 441, 18
- McKee, C. F. & Krumholz, M. R. 2010, *ApJ*, 709, 308
- Menanteau, F., Ford, H. C., Motta, V., Benítez, N., Martel, A. R., Blakeslee, J. P., & Infante, L. 2006, *AJ*, 131, 208
- Mihos, J. C. & Hernquist, L. 1996, *ApJ*, 464, 641
- Morgan, W. W. & Mayall, N. U. 1957, *PASP*, 69, 291
- Morris, J. & Monaghan, J. 1997, *Journal of Computational Physics*, 136, 41
- Murali, C., Katz, N., Hernquist, L., Weinberg, D. H., & Davé, R. 2002, *ApJ*, 571, 1
- Narayanan, D., Dey, A., Hayward, C. C., Cox, T. J., Bussmann, R. S., Brodwin, M., Jonsson, P., Hopkins, P. F., Groves, B., Younger, J. D., & Hernquist, L. 2010a, *MNRAS*, 407, 1701
- Narayanan, D., Hayward, C. C., Cox, T. J., Hernquist, L., Jonsson, P., Younger, J. D., & Groves, B. 2010b, *MNRAS*, 401, 1613
- Oppenheimer, B. D. & Davé, R. 2008, *MNRAS*, 387, 577
- Patel, S. G., van Dokkum, P. G., Franx, M., Quadri, R. F., Muzzin, A., Marchesini, D., Williams, R. J., Holden, B. P., & Stefanon, M. 2013, *ApJ*, 766, 15
- Planck Collaboration, Ade, P. A. R., Aghanim, N., Armitage-Caplan, C., Arnau, M., Ashdown, M., Atrio-Barandela, F., Aumont, J., Baccigalupi, C., Banday, A. J., & et al. 2013, *ArXiv e-prints:1303.5076*
- Robertson, B., Yoshida, N., Springel, V., & Hernquist, L. 2004, *ApJ*, 606, 32
- Robertson, B. E. & Kravtsov, A. V. 2008, *ApJ*, 680, 1083
- Rodighiero, G., Daddi, E., Baronchelli, I., Cimatti, A., Renzini, A., Aussel, H., Popesso, P., Lutz, et al. 2011, *ApJL*, 739, L40

- Saitoh, T. R. & Makino, J. 2009, *ApJL*, 697, L99  
— 2013, *ApJ*, 768, 44
- Sanders, D. B. & Mirabel, I. F. 1996, *ARA&A*, 34, 749
- Schaye, J. & Dalla Vecchia, C. 2008, *MNRAS*, 383, 1210
- Schmidt, M. 1959, *ApJ*, 129, 243
- Sérsic, J. L. 1963, *Boletín de la Asociación Argentina de Astronomía La Plata Argentina*, 6, 41
- Snyder, G. F., Lotz, J., Moody, C., Peth, M., Freeman, P., Ceverino, D., Primack, J., & Dekel, A. 2015, *MNRAS*, 451, 4290
- Somerville, R. S., Barden, M., Rix, H.-W., Bell, E. F., Beckwith, S. V. W., Borch, A., Caldwell, J. A. R., Häußler, B., Heymans, C., Jahnke, K., Jogee, S., McIntosh, D. H., Meisenheimer, K., Peng, C. Y., Sánchez, S. F., Wisotzki, L., & Wolf, C. 2008, *ApJ*, 672, 776
- Somerville, R. S., Popping, G., & Trager, S. C. 2015, *ArXiv e-prints*:1503.00755
- Sparre, M., Hayward, C. C., Springel, V., Vogelsberger, M., Genel, S., Torrey, P., Nelson, D., Sijacki, D., & Hernquist, L. 2015, *MNRAS*, 447, 3548
- Speagle, J. S., Steinhardt, C. L., Capak, P. L., & Silverman, J. D. 2014, *ApJS*, 214, 15
- Springel, V. 2005, *MNRAS*, 364, 1105
- Springel, V. & Hernquist, L. 2003, *MNRAS*, 339, 289
- Stadel, J. G. 2001, PhD thesis, UNIVERSITY OF WASHINGTON
- Stark, D. P., Schenker, M. A., Ellis, R., Robertson, B., McLure, R., & Dunlop, J. 2013, *ApJ*, 763, 129
- Stefanon, M., Marchesini, D., Rudnick, G. H., Brammer, G. B., & Whitaker, K. E. 2013, *ApJ*, 768, 92
- Stott, J. P., Sobral, D., Smail, I., Bower, R., Best, P. N., & Geach, J. E. 2013, *MNRAS*, 430, 1158
- Stringer, M., Trujillo, I., Dalla Vecchia, C., & Martínez-Valpuesta, I. 2015, *MNRAS*, 449, 2396
- Tacconi, L. J., Neri, R., Genzel, R., Combes, F., Bolatto, A., Cooper, M. C., Wuyts, S., Bournaud, F., et al. 2013, *ApJ*, 768, 74
- Tassis, K., Gnedin, N. Y., & Kravtsov, A. V. 2012, *ApJ*, 745, 68
- Thompson, R. 2014, *pyGadgetReader: GADGET snapshot reader for python*, *Astrophysics Source Code Library*:1411.001
- 2015, *SPHGR: Smoothed-Particle Hydrodynamics Galaxy Reduction*, *Astrophysics Source Code Library*:1502.012
- Thompson, R., Davé, R., & Nagamine, K. 2015, *MNRAS*, 452, 3030
- Thompson, R., Nagamine, K., Jaacks, J., & Choi, J.-H. 2014, *ApJ*, 780, 145
- Toomre, A. & Toomre, J. 1972, *ApJ*, 178, 623
- van Dokkum, P. G., Bezanson, R., van der Wel, A., Nelson, E. J., Momcheva, I., Skelton, R. E., Whitaker, K. E., Brammer, et al. 2014, *ApJ*, 791, 45
- van Dokkum, P. G. & Brammer, G. 2010, *ApJL*, 718, L73
- Watson, D. 2011, *A&A*, 533, A16
- Wellons, S., Torrey, P., Ma, C.-P., Rodriguez-Gomez, V., Vogelsberger, M., Kriek, M., van Dokkum, P., Nelson, E., Genel, S., Pillepich, A., Springel, V., Sijacki, D., Snyder, G., Nelson, D., Sales, L., & Hernquist, L. 2015, *MNRAS*, 449, 361
- Wiersma, R. P. C., Schaye, J., Theuns, T., Dalla Vecchia, C., & Tornatore, L. 2009, *MNRAS*, 399, 574
- Zolotov, A., Dekel, A., Mandelker, N., Tweed, D., Inoue, S., DeGraf, C., Ceverino, D., Primack, J. R., Barro, G., & Faber, S. M. 2015, *MNRAS*, 450, 2327